Image Registration with Homography: A Refresher with Differentiable Mutual Information, Ordinary Differential Equation and Complex Matrix Exponential

by

Abhishek Nan

A thesis submitted in partial fulfillment of the requirements for the degree of

Master of Science

Department of Computing Science

University of Alberta

Abstract

This work presents a novel method of tackling the task of image registration. Our algorithm uses a differentiable form of Mutual Information implemented via a neural network called MINE. An important property of neural networks is them being differentiable, which allows them to be used as a loss function. This way we use MINE as an estimator for our loss function. Furthermore to make the optimization smoother, we parametrize the transformation module using complex matrix manifolds which further improves our accuracy and efficiency. In order to speed up computation and make the algorithm more robust we use a multi-resolution approach, but implement it as a simultaneous loss from all levels, which provides the aforementioned benefits. The parameters for each resolution are modelled via ordinary differential equations and solved using a neural network which adds to the final performance scores as well. This leads to a state of the art algorithm implemented via modern software frameworks which allow for automatic gradient computations (such as PyTorch). Our algorithm performs better than registration algorithms available off the shelf in state of the art image registration tools/softwares. We demonstrate this on four open source datasets. The source code is publicly available on Github[1].

[1]Link to source code: https://github.com/abnan/ODECME

Preface

This is a collaborative work with Dr. Nilanjan Ray and Dr. Matthew Tennant. Parts of this thesis have been submitted to Medical Imaging with Deep Learning (MIDL 2020) and IEEE Transactions on Medical Imaging (IEEE TMI). These submissions were co-authored with Dr. Nilanjan Ray, Dr. Matthew Tennant and Dr. Uriel Rubin.

To my parents

For being a constant source of inspiration.

I could either watch it happen or be a part of it.

– Elon Reeve Musk, 2019.

Acknowledgements

I would like to thank Dr. Nilanjan Ray. His guidance throughout the period of my program made this work possible. I owe a debt of gratitude to my parents who supported my decision to move away far from home in pursuit of furthering my education. They have been a source of constant inspiration and strength throughout. Last, but not least, I would also like to express my gratitude to Dr. Matt Tennant for his continued support.

This work was supported in part by NSERC Discovery Grants.

Contents

List of Tables

List of Figures

Chapter 1

Introduction

1.1 Problem definition

Image registration is the task of finding the correspondences across two or more images and bringing the images into a single coordinate system. This is often used to tackle problems in the field of medical imaging, remote sensing, etc. For instance, in case we want to analyse how the anatomy of a patient's body part changes over time, we need snapshots of it over time. Not only could the source camera change, the location, orientation of the camera as well as of the patient are variables that could change over time. In such scenarios, doing a comprehensive analysis becomes difficult and hence, registration becomes a prerequisite before any further analysis can be done. For instance, Figure 1.1 shows two images from the FIRE (Fundus Image Registration Dataset)[31] dataset. They are snapshots of the same patient's retinal fundus taken few months apart. The white spots show corresponding anatomical points which should ideally be completely overlapping, but aren't due to changes over time. Hence, they need to be registered before further analysis. In this thesis, we tackle this problem of pairwise registration, where we try to find the points of correspondence between such a pair of images.

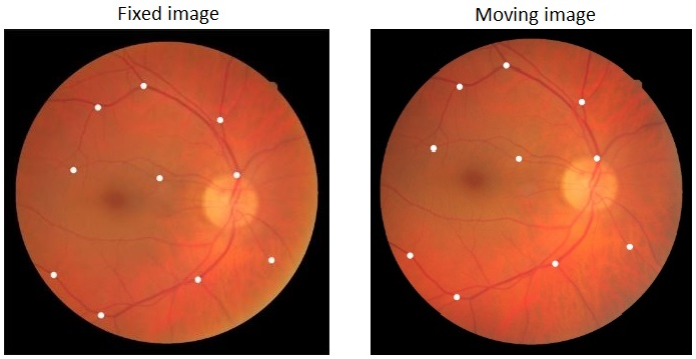

Figure 1.1: A pair of images from the FIRE dataset with the ground truth depicted as white spots.

In this thesis, we primarily deal with homography based registration. Before we proceed further, we first define homography; any two images of the same planar surface in space are said to be related by a homography. A homography has 8 degrees of freedom and it relates the transformation between two planes using the following equation (where x and y are co-ordinates of a pixel in the original plane and x' and y' are the same pixel's co-ordinates in the transformed plane):

$$\begin{bmatrix} X \\ Y \\ Z \end{bmatrix} = \begin{bmatrix} H_{11} & H_{12} & H_{13} \\ H_{21} & H_{22} & H_{23} \\ H_{31} & H_{32} & 1 \end{bmatrix} \begin{bmatrix} x \\ y \\ 1 \end{bmatrix}, \; x' = \frac{X}{Z}, \; y' = \frac{Y}{Z}. \tag{1.1}$$

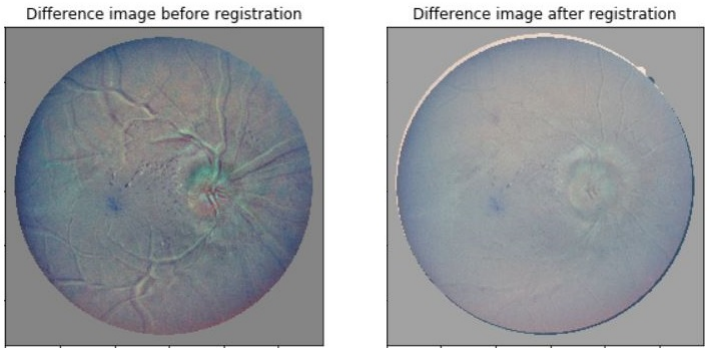

Figure 1.2: A pair of images from the FIRE dataset

In terms of registration, the moving image is transformed using a homography to minimize a distance metric between the fixed and the moving image.

For instance, in Fig. 1.1 we transform the moving image using the homography $\begin{bmatrix} 1.00 & 6.64 & -0.01 \\ -0.06 & 1.00 & 6.81 \\ 2.55 & -3.7e-06 & 1 \end{bmatrix}$ and Fig. 1.2 shows the difference image between the fixed image and the moving image before and after the homography transformation is applied.

While there are multiple approaches to image registration, they may be broadly classified into two families based on how the registration parameters are obtained: learning based and optimization based. While the benefit of learning based approaches is that once trained on a dataset, inference is quite fast. On the other hand, the drawback of learning based approaches is that they need large amounts of training data to achieve satisfactory results and furthermore, they won't perform well on pairs which are drastically different from the training set. Hence, here we try to present an optimization based approach using which inference might be slightly longer than learning based methods, but they are very robust and work on any image sets and do not require annotated training data at all.

1.2 Significance of problem

In the field of fundoscopy, microvascular circulation is observed to diagnose and monitor diseases such as diabetes and hypertension[29]. For accurate observations, image registration is a necessary prerequisite. Also due to progression or remission of retinopathy, there might be structural changes in the retina. In such a case where images from the same camera source are registered, it is called mono-modal registration. Once image registration has been performed, the images can subsequently be used for super-resolution, mosaicing and longitudinal studies.

Furthermore, the camera source need not always be the same. Different imaging modalities can provide different and additive information for the clinician or researcher regarding human tissue. For example, radiation of different wavelengths are able to penetrate human tissues to differing depths. A particular wavelength might be used to produce a map of bone structure, while

a different wavelength could be used to map other internal organs. These two different maps are referred to as different modalities. A common way to perform a holistic analysis is to combine the (complimentary) information from these different modalities. Alignment of the different modalities requires multi-modal registration. But registering such cross-modal images requires techniques quite different from mono-modal registration.

In general, the problem of registration is not just limited to the domain of medical imaging, but is quite pervasive in many domains of digital image processing. For instance, in the robotics community it is framed as the problem of template matching, where the objective is to find an object in different scenes. This could be used for tasks such as object localization [25, 21] or object tracking [14].

Furthermore, to tackle the problem of image registration, often the model used to parametrize the registration parameters are fashioned in a hierarchical manner; i.e. first a global transformation using homography (or its subsets) is used to register the images as much as possible before applying more elaborate techniques such as deformable registration. Thus, the success of deformable registration methods is highly dependent on how successful the initial registration step was. Our optimization based registration approach tries to improve this initial global homography based registration.

1.3 Motivation

One of the most successful metrics used for cross-modal or multi-modal medical image registration is mutual information (MI) [57]. In the context of scalar-valued images, these joint probabilities are calculated using a two-dimensional histogram of the two images. Most current MI-based techniques for registration use slight variations of the above method to approximate MI. While this works well, there are some issues associated with this method of evaluation as follows.

- The number of histogram bins chosen becomes a hyperparamter. While increasing the number of bins would lead to better accuracy in computa-

tion, this comes at the cost of time. Furthermore, there is no theoretical upper bound on the number of bins that should be used for accurate results.

- Images with higher dimensions (color images, hyper-spectral images), would need a higher dimensional histograms and a joint histogram requiring a very large sample that is often computationally prohibitive. For instance, an RGB image has 3 channels and that would need a 6-dimensional joint histogram. A common way to bypass this restriction is to work with grayscale intensities of images, but this leads to loss of valuable information, incorporating which would very likely have led to better results.

Furthermore, even though several software toolboxes exist for optimization-based image registration using the family of homography transformations, we believe that opportunities still exist for improvement. It is quite common to see the homography matrix parameters themselves being optimized, even though it has been seen that it leads to quite poor performance [18]. We explore alternative methods of parametrizing the homography transformation in an effort to improve performance.

Since most optimization based registration frameworks use a multiresolution approach, the image structures are slightly shifted throughout the pyramid. This implies that the idea of using the same parameters [71] for all levels for registration can be improved upon.

1.4 Thesis contribution

To tackle the issues of histogram-based Mutual Information computation as discussed in the previous section, we bring in a neural network based Mutual Information estimator (MINE). This has the added benefit of being differentiable.

Next, we look at the problem of parametrization. While previous attempts have been made to parametrize the homography transformation differently,

there exist very limited attempts at doing so via matrix exponential[80]. In this work, we point out that representing transformation matrices using a matrix exponential, especially, complex matrix exponential (CME) leads to faster convergence. CME enjoys a theoretical guarantee that repeated compositions of matrix exponential are not required during optimization, unlike the real case. Furthermore, using a matrix exponential, both the forward and the reverse transformations can be easily added to the registration objective function for a robust design.

Finally, we tackle the problem of using different registration coefficients for different levels of the multi-resolution registration. We posit that a precise design of transformation matrix is possible for the multi-resolution image registration using a dynamical system modeled by a neural network. This dynamical system leads to an initial value ordinary differential equations (ODE) that can adapt a transformation matrix quite accurately to the multi-resolution image pyramids, which are significant for image registration. This ODE-based framework leads to a more accurate image registration algorithm. Our work also demonstrates the simplicity of modelling the dynamics via a neural network. Thanks to software which allow automatic gradient computation, it becomes trivial to optimize the parameters for this neural network.

This thesis makes three primary contributions:

1. The original MINE implementation was proposed as a general purpose Mutual Information estimator for n-dimensional variables. This work presents one of the first applications of using MINE for images and volumetric data. We perform large scale experiments with multiple 2D and 3D datasets showing its utility as a differentiable cost function which can be used for image registration.

2. Our work demonstrates the potential benefits of using complex matrix exponential, both theoretically as well as empirically. Furthermore, leveraging the fact that we use matrix exponentials, it becomes trivial to compute the inverse transformation and introduce a more robust symmetric loss function.

3. This thesis also presents the novel idea of modelling the dynamics of the coefficients of the matrix exponentials across different levels of the multi-resolution pyramid as an initial value problem, which is then solved using numerical methods for solving ordinary differential equations.

   Using the aforementioned elements, the symmetric cost function, ODE and CME, we present a novel multi-resolution image registration algorithm ODECME that can accommodate both 2D and 3D image registration, mono-modal and multi-modal [57] cases, and any differentiable loss or objective function including MINE (mutual information neural estimation) [8]. (A previous iteration of the algorithm called DRMIME is also presented, which lacks the symmetric loss function, ODE and CME components).

   We frame the classical problem of image registration in the context of optimization as many have done before, but thanks to the evolution of modern frameworks such as PyTorch [56] which allow automatic gradient computation, we are able to leverage some of the aforementioned ideas and incorporate them, most of which would have been tremendously difficult without the existence of such software frameworks. Furthermore, these frameworks also have features such as GPU acceleration, which allow us to better leverage technological advances in computing hardware as well.

1.5 Organization of the Thesis

- **Chapter 1.** *Introduction*

  We introduce the problem, the motivation behind it, and the potential gaps in approaches to solving it that can be addressed.

- **Chapter 2.** *Background*

  We provide an overview of different ideas that will be eventually used to build our final algorithm.

- **Chapter 3.** *Related Works*

  In this section we talk about the alternative families of approaches that were used to tackle the image registration problem.

- **Chapter 4.** *Proposed Multi-Resolution Image Registration*

  Here we describe the individual ideas introduced in our thesis and how they all come together for our proposed DRMIME/ODECME algorithm.

- **Chapter 5.** *Experiments*

  We first talk about the datasets we used for evaluating our aforementioned method. Then we discuss our experiments and how we use them to evaluate our methodology against standard approaches.

- **Chapter 6.** *Conclusion*

  We present the conclusions of this thesis and summarize the ideas newly introduced here.

- **Chapter 7.** *Appendix*

  This section lists the hyperparameters for the different algorithms that were used.

Chapter 2

Background

2.1 Optimization for Image Registration

Let us denote by T the fixed image and by M the moving image to be registered. Let H denote a transformation matrix signifying affine or homography or rigid body or any other suitable transformation. Further, let $Warp(M, H)$ denote an interpolation function that transforms the moving image M by a transformation matrix H. Optimization-based image registration minimizes the following objective function to find the optimum transformation matrix H that aligns the transformed moving image with the fixed image:

$$\min_{H} D(T, Warp(M, H)), \tag{2.1}$$

where D is a loss function that typically measures a distance between the fixed and the warped moving image. There can be many different loss functions D, but to stay relevant to this work we only discuss Mean Square Error and why Mutual Information is needed.

2.1.1 Mean Square Error

When two images are of the same modality, i.e. taken using the same source camera, it is intuitive that we will find the exact same components of the moving image in the target image. So when registered with each other, if we take the difference between the two images, due to this complete overlap the difference will be minimal and if not registered, the difference value would be higher. Mean Square Error is such a cost function which utilises this property.

Eqn. 2.1 now becomes:

$$\min_{H} \frac{1}{n} \sum_{x,y} (T[x][y] - Warp(M, H)[x][y])^2 \tag{2.2}$$

where n is the number of pixels. Eqn. 2.2 has the benefit of being differentiable as well as accentuating larger differences as compared to smaller ones. Often gradient descent based techniques can be used for such intensity-based measures to find the correct registration parameters [42]. This can also be framed as a supervised learning problem [18], where the goal is to learn the parameters of the homography transformation.

2.1.2 Mutual Information

Since different modalities can have different image intensities and varying contrast levels between them, it is unlikely that using MSE as a registration metric will work well. Even on complete overlap/registration, the Mean Squared Error between the two images won't be minimized. For ex. Figure 2.1 shows a CT scan and an MR scan in the left and middle figures respectively. It is intuitive to see how we need a different cost function here. One of the most common metrics used in multi-modality registration is mutual information (MI).

In the field of information theory, Mutual Information (MI) is a metric commonly used to compute the dependence between two variables. As the name says intuitively, $MI(X, Y)$ tells us how much *information* about X is shared by Y. Also as obvious from the term *Mutual* Information, the information shared by X about Y is the same as the information shared by Y about X. Two highly dependent variables will have a high MI score, while two less dependent variables will have a low MI score.

Mathematically, it has come to be expressed in various equivalent forms and we'll discuss three of them here. Each definition is correct in its own right, and all three can be used interchangeably and rewritten as the other. Also since this work deals with image registration in general, we will look at Mutual Information from the perspective of images. For the first form, given images X and Y, we can define Mutual Information between them as

$$MI(X, Y) = H(X) - H(X|Y) \tag{2.3}$$

Figure 2.1: Example of joint histogram involved in MI computation for multi-modal images. The image on the left is a CT scan and the middle is a MR scan. The image on the right is a joint histogram with the grey values of the CT scan on the x-axis and the MR scan on the y-axis. For each (x,y) co-ordinate in the histogram, if they are corresponding points from the CT image and MR image respectively, the intensity at point (x,y) is increased. Source: Pluim, Maintz, and Viergever [57]

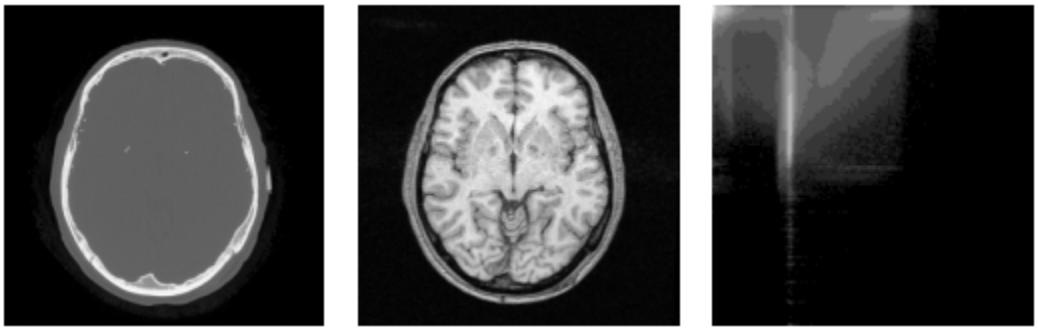

where H(x) is the Shannon entropy of image X, which is computed by considering the probability distribution of the greyscale pixel values. $H(X|Y)$ is the conditional entropy which is computed using $p(x|y)$, i.e. the probability of grey value x in image X given that the corresponding pixel in image Y has intensity value y. Alternatively, we could also state MI as the amount by which the uncertainty about X decreases when Y is given. Thinking of this idea in terms of image registration, it is intuitive to see that the mutual information between two images is maximised when they are registered.

The second way of defining MI is as follows:

$$MI(X,Y) = H(X) + H(Y) - H(X,Y) \tag{2.4}$$

The term $H(X,Y)$ refers to joint entropy and as such, if we are trying to maximise $MI(X,Y)$ we want to minimize the joint entropy. An issue with using just joint entropy for image registration is that this value can be low even in the case of un-registered images. For instance, suppose after a transformation, only some part of the background overlaps between two images. Even in such a case, the joint histogram will be very sharp despite the misalignment. Since Mutual Information uses the marginal entropies as well ($H(X)$ and $H(Y)$), these will have low values when the overlapping part of the images contains

only the background. Only in case of high anatomical overlap will it have a high value.

The final form of Mutual Information is formulated using the Kullback-Leibler(KL) distance. The KL divergence between two distributions p and q is defined as:

$$\sum_i p(i) log \frac{p(i)}{q(i)} \tag{2.5}$$

Similarly, the Mutual Information between two images X and Y is defined as:

$$MI(X,Y) = \sum_{x,y} p(x,y) log \frac{p(x,y)}{p(x)p(y)}. \tag{2.6}$$

It is fairly intuitive to understand how we arrived here from the KL-divergence formulation. Since we want to understand the dependance between the two images, we compute the KL-divergence between the joint distribution of the images' grey values p(x,y) and the joint distribution in case of independence of the two images, i.e. $p(x)p(y)$. In case the images are correctly aligned, we will have maximal dependence.

Mutual Information is also a symmetric measure, i.e., $MI(X,Y) = MI(Y,X)$. Furthermore, it is bounded by zero on the lower end in case of complete independence between two variables and it does not have a upper bound. Hence, it is used as a relative measure.

We first saw [59] such a measure in Woods, Cherry, and Mazziotta [83] that was based on the intuition that areas of similar tissue (and by extension areas of similar greyscale intensity) in a reference image would correspond to areas of similar intensity in the moving image. The average variance of this ratio for all parts of the image was minimised to achieve registration.

Figure 2.2: Joint histogram of an image with itself. (Source: Pluim, Maintz, and Viergever [59]) The leftmost is the unchanged image with itself and as we go right, it depicts the joint histogram of the image with a version of it that has been rotated by angles of 2, 5 and 10 degree respectively. Below the histograms are the joint entropy values.

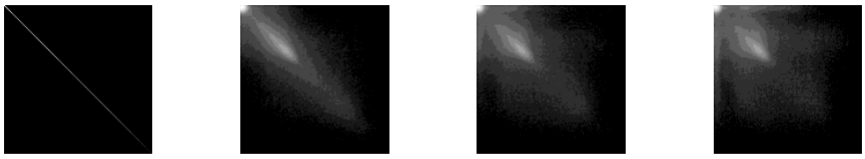

Hill et al. [32] built on the same idea and proposed an extension where they plot a two-dimensional joint histogram of grey values in each of the two images for all corresponding points (Figure 2.2). When two images are registered, corresponding anatomical regions will overlap and certain clusters will show up with the grey values of those regions. When images are not yet registered, different anatomical parts might overlap non-corresponding parts in the other image. In such a case, the intensity of the clusters for the corresponding anatomical structures will decrease, since new combinations of intensity values will emerge, for eg. skull and brain in MRI images. In the joint histogram, this appears as a dispersion of clusters. Using these characteristics, Hill et al. used the third order moment of the joint histogram, which tells us the skewness of the distribution.

Collignon et al. [16] and Studholme, Hill, and Hawkes [69] on the other hand suggested the use of entropy as a measure for image registration. Entropy measures the dispersion of a probability distribution. In partricular, Shannon entropy for a joint distribution is defined as:

$$-\sum_{x,y} p(x,y) log p(x,y). \tag{2.7}$$

Entropy is low when when there a few sharply defined peaks in the histogram and it is high when all outcomes have similar probabilities. A joint histogram of two images can be used to estimate a joint probability distribution of their grey values by dividing each entry in the histogram by the total number of entries. This idea finally led to the conceptualization of mutual information as

a metric for multi-model registration. This method was introduced by Viola and Wells III [79, 81].

2.1.3 Mutual Information Neural Estimation

As stated before (Eqn. 2.3) Mutual Information presents the dependence between two variables X and Z. Also as we have seen according to Eqn. 2.6, the MI is equivalent to the Kullback-Liebler (KL-) divergence between the joint distribution ($P_{x,z}$) and product of the marginals ($P_x P_z$).

According to the Donsker-Varadhan (DV) representation[19], we have the following dual representation of KL-divergence:

$$D_{KL}(X||Z) = sup_{T:\Omega \to R} E_X[T] - log(E_Y[e^T]) \tag{2.8}$$

where the supremum is taken over all functions T such that the two expectations are finite.

As a result of this, we have the following the following lower bound [5]:

$$D_{KL}(X||Z) \geq sup_{T \in F} E_X[T] - log(E_Z[e^T]) \tag{2.9}$$

Where F is any class of functions $T : \Omega \to R$ which satisfies the integrability constraints of the theorem. This bound is tight for optimal density functions $T*$ that relate to the *Gibbs density* as,

$$dP = \frac{1}{Z} e^T dQ, \text{ where } Z = E_Q[e^{T*}]$$

Using Eqn. 2.6 and the dual representation of the KL-divergence, Belghazi et al. [8] choose the function F to be the family of functions $T_\theta : X \times Z \to R$ parametrized by a deep neural network with parameters θ. The network is called the statistics network and this measure is called the *neural information measure.*

So overall, we have:

$$MI = \sup_f J(f), \tag{2.10}$$

where $J(f)$ is the DV lower bound:

$$J(f) = \int f(x,z)P_{XZ}(x,z)dxdz - \\ log(\int exp(f(x,z))P_X(x)P_Z(z)dxdz). \tag{2.11}$$

Figure 2.3: MINE as proposed by Belghazi et al. in [8]

Algorithm 1 MINE

$\theta \leftarrow$ initialize network parameters
repeat
Draw b minibatch samples from the joint distribution:
$(\boldsymbol{x}^{(1)}, \boldsymbol{z}^{(1)}), \ldots, (\boldsymbol{x}^{(b)}, \boldsymbol{z}^{(b)}) \sim \mathbb{P}_{XZ}$
Draw n samples from the Z marginal distribution:
$\bar{\boldsymbol{z}}^{(1)}, \ldots, \bar{\boldsymbol{z}}^{(b)} \sim \mathbb{P}_Z$
Evaluate the lower-bound:
$\mathcal{V}(\theta) \leftarrow \frac{1}{b}\sum_{i=1}^{b} T_\theta(\boldsymbol{x}^{(i)}, \boldsymbol{z}^{(i)}) - \log(\frac{1}{b}\sum_{i=1}^{b} e^{T_\theta(\boldsymbol{x}^{(i)}, \bar{\boldsymbol{z}}^{(i)})})$
Evaluate bias corrected gradients (e.g., moving average):
$\widetilde{G}(\theta) \leftarrow \widetilde{\nabla}_\theta \mathcal{V}(\theta)$
Update the statistics network parameters:
$\theta \leftarrow \theta + \widetilde{G}(\theta)$
until convergence

Using this differentiable form of MI, we can reframe our optimization objective from Eqn. 2.1 as:

$$\max_H MINE(T, Warp(M, H)). \tag{2.12}$$

2.2 Multi-resolution Computation

A problem with gradient based methods is that they are highly dependent on initialization and step-size parameters. An alternative approach is to use evolutionary algorithms and/or search heuristics[78]. While both methods have their pros and cons, a lot of modern day machine learning research is focused on developing optimizers for gradient descent and as such is a promising approach. A technique which ameliorates the issues with gradient based methods are multi-resolution pyramids[75, 43, 2]. The idea behind the approach is very

Figure 2.4: Multi-resolution pyramid (Source: Wikipedia)

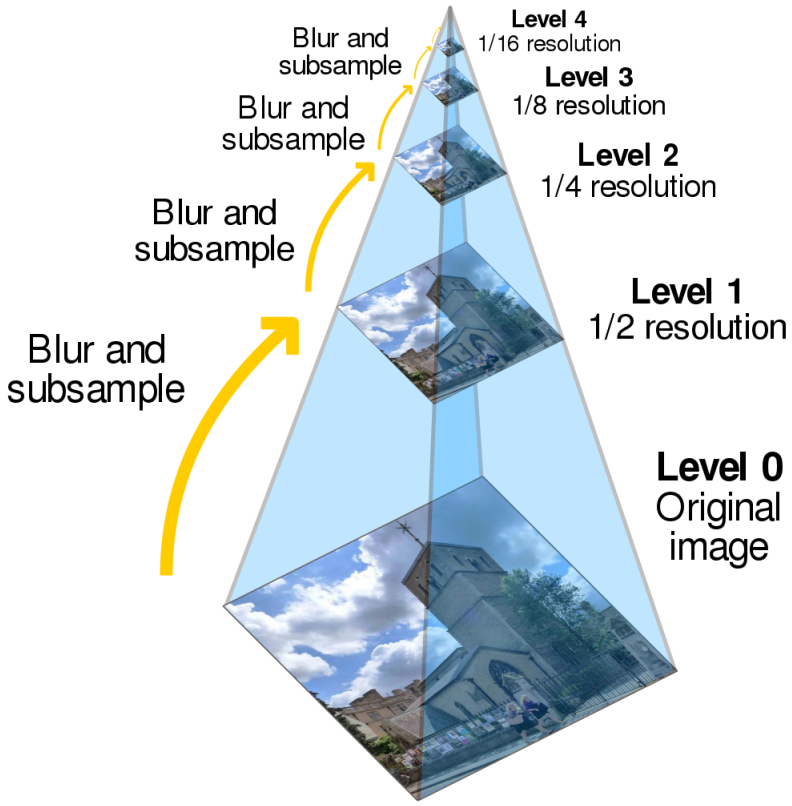

intuitive; a Gaussian pyramid of images is constructed where the original image lies at the bottom level and subsequent higher levels have a down-scaled, Gaussian blurred version of the image. This not only serves to simplify the optimization, but also serves to speed it up since at the coarsest level the size of the data is greatly reduced making each iteration of gradient descent much faster.

While mutual information works quite well for multi-modality registration, often due to its high complexity, practitioners resort to using such a multi-resolution approach. One of the earliest applications of this was by Wells III et al. [81], where they observed that using such an approach resulted in there being less of a tendency of the optimization getting stuck in a local minima, but this came at the cost of reduced accuracy. This comes from the idea that using a lower resolution version of the image increases the capture range [33]. The capture range is defined as a range within which a randomly initialized

algorithm is likely to converge to the correct optimum. But the idea has proved to be a bit controversial over time. Results by Pluim, Maintz, and Viergever [58] and Wu and Chung [84] claim that even with a multi-resolution approach the capture range might still not be good enough. The statistical measure that Mutual Information computes decreases as image resolution decreases[34]. So just using a multi-resolution framework in itself is not a very robust approach.

Alternate approaches have tried to combine different losses with Mutual Information to add robustness. For instance, Wu and Chung used a combined loss of MI and Sum of Difference (SAD) along with their multi-resolution approach. Sun et al. [71] proposed alternative ideas of multi-resolution strategies for the both the data and transformation models. They used the simultaneous loss from multiple levels rather than solving for each level subsequently. Computing the aggregate loss was done using two approaches, either the 'Sum' or the 'Union'. In case of the former, the losses from each level was computed separately and all losses simply added up. In case of the 'Union' approach, a single loss was computed by combining the fixed-moving pairs from the coarse and fine multi-resolution levels. In case of measures such as Mean Square Error, the 'Sum' and 'Union' approaches are equivalent; but in cases where the cost function is normalized correlation coefficient (NCC) or mutual information (MI), they both lead to different computations.

To make things more concrete; Using a multi-resolution recipe, two image pyramids are built: T_l and M_l for $l = 1, ..., L$, where L is the maximum level in the pyramid. Here, $T_1 = T$ and $M_1 = M$ are the original fixed and moving images, respectively. Then, a registration problem (2.1) takes the following form:

$$\min_{H} \sum_{l=1}^{L} D(T_l, Warp(M_l, H))). \tag{2.13}$$

The usual practice for a multi-resolution approach is to start computation at the highest (i.e., coarsest) level of the pyramid and gradually proceed to the original resolution. In contrast, we found that working simultaneously on all the levels as captured in the optimization problem (2.13) is more beneficial.

2.3 Matrix Exponential

The optimization problem (2.1) can be carried out by gradient descent once we are able to compute the gradient of the loss function D with respect to H. The implicit assumption here is that the loss function D is differentiable and so are the computations within $Warp$. However, an additional technical difficulty arises in gradient computation when the elements of the transformation matrix H are constrained, as in rigid-body transformation. In such cases, matrix exponential provides a remedy. For example, finding the parameters for rigid transformation can be seen as an optimization problem on a finite dimensional Lie group [62]. In the robotics community, this is a fairly common technique used for the problem of template matching.

One of the earliest works by Taylor and Kriegman [74] shows how to perform optimization procedures over the Lie group *SO(3)* (*SO(3)* is the group of rotations in 3D space) and related manifolds. Their work motivates how any arbitrary geometric transformation has a natural parametrization based on the exponential operator associated with the respective Lie group. They also proved how such a technique is more effective than other methods which approximate gradient descent on the tangent space to the manifold. This was also extended to deformable pattern matching [77]. Among more recent work, data representations in orientation scores, which are functions on the Lie group *SE(2)* (*SE(2)* is the group of rigid transformations in the 2D plane) were used for template matching[7] via cross-correlation.

Wachinger and Navab [80] state that spatial transformations parametrized with Lie groups help because 3D rigid transformations do not form a vector space. They also use optimize using local canonical coordinates which has the benefit that the geometric structure of the group is taken care of implicitly. This enables them to frame the problem as an unconstrained optimization.

We make things a bit more concrete before moving further. *Aff(2)* is the group of affine transformations on the 2D plane. There are six degrees of freedom in this group: two for translation, one for rotation, one for scale, one for stretch, one for shear; hence this group has 6 generators:

$$B_1 = \begin{bmatrix} 0 & 0 & 1 \\ 0 & 0 & 0 \\ 0 & 0 & 0 \end{bmatrix}, B_2 = \begin{bmatrix} 0 & 0 & 0 \\ 0 & 0 & 1 \\ 0 & 0 & 0 \end{bmatrix}, B_3 = \begin{bmatrix} 0 & 1 & 0 \\ 0 & 0 & 0 \\ 0 & 0 & 0 \end{bmatrix},$$
$$B_4 = \begin{bmatrix} 0 & 0 & 0 \\ 1 & 0 & 0 \\ 0 & 0 & 0 \end{bmatrix}, B_5 = \begin{bmatrix} 1 & 0 & 0 \\ 0 & -1 & 0 \\ 0 & 0 & 0 \end{bmatrix}, B_6 = \begin{bmatrix} 0 & 0 & 0 \\ 0 & -1 & 0 \\ 0 & 0 & 1 \end{bmatrix}.$$

The exponential map for this group has no closed form. Any general matrix exponential routine can be used for this purpose. If $v = [v_1, v_2, ..., v_6]$ is a parameter vector, then the affine transformation matrix is obtained using the expression: $Mexp(\sum_{i=1}^{6} v_i B_i)$, where $Mexp$ is the matrix exponentiation operation that can be computed by either (E is an identity matrix):

$$Mexp(B) = \lim_{n \to \infty} (E + \frac{1}{n} B)^n, \tag{2.14}$$

or,

$$Mexp(B) = \sum_{n=0}^{\infty} \frac{B^n}{n!}. \tag{2.15}$$

There are several other ways to compute the matrix exponential [52], and our only requirement is the expression be differentiable. In DRMIME/ODECME we use the series (2.15) for matrix exponential. We truncate the series after 10 terms and empirically find that this choice yields good registration accuracy.

Similarly, *SL(3)* is the group of transformations representing homographies on the 2D projective plane. There are eight degrees of freedom in this group: two for translation, one for rotation, one for scale, one for shear, one for stretch and two for perspective change; its generators are:

$$B_1 = \begin{bmatrix} 0 & 0 & 1 \\ 0 & 0 & 0 \\ 0 & 0 & 0 \end{bmatrix}, B_2 = \begin{bmatrix} 0 & 0 & 0 \\ 0 & 0 & 1 \\ 0 & 0 & 0 \end{bmatrix}, B_3 = \begin{bmatrix} 0 & -1 & 0 \\ 1 & 0 & 0 \\ 0 & 0 & 0 \end{bmatrix},$$
$$B_4 = \begin{bmatrix} 1 & 0 & 0 \\ 0 & 1 & 0 \\ 0 & 0 & -2 \end{bmatrix}, B_5 = \begin{bmatrix} 1 & 0 & 0 \\ 0 & -1 & 0 \\ 0 & 0 & 0 \end{bmatrix}, B_6 = \begin{bmatrix} 0 & 1 & 0 \\ 1 & 0 & 0 \\ 0 & 0 & 0 \end{bmatrix},$$
$$B_7 = \begin{bmatrix} 0 & 0 & 0 \\ 0 & 0 & 0 \\ 1 & 0 & 0 \end{bmatrix}, B_8 = \begin{bmatrix} 0 & 0 & 0 \\ 0 & 0 & 0 \\ 0 & 1 & 0 \end{bmatrix}.$$

Using the matrix exponential representation for a transformation matrix, $H = Mexp(\sum_{i=1}^{6} v_i B_i)$, the image registration optimization defined in (2.1) takes the following form:

$$\min_{v_1,\ldots,v_6} D(T, Warp(M, Mexp(\sum_{i=1}^{6} v_i B_i))). \tag{2.16}$$

We can now apply standard mechanisms of gradient computation $\frac{\partial D}{\partial v_i}$ by automatic differentiation (i.e., chain rule) and adjust parameters v_i by gradient descent.

Similarly for volumetric (3D) data, we can have the *SE(3)* and *Sim(3)* groups. The *SE(3)* group represents all 3D rigid transformations, i.e. it has six degrees of freedom, which are the three axes of rotation and three directions of translation. The six generators [20] are:

$$B_1 = \begin{bmatrix} 0 & 0 & 0 & 1 \\ 0 & 0 & 0 & 0 \\ 0 & 0 & 0 & 0 \\ 0 & 0 & 0 & 0 \end{bmatrix}, B_2 = \begin{bmatrix} 0 & 0 & 0 & 0 \\ 0 & 0 & 0 & 1 \\ 0 & 0 & 0 & 0 \\ 0 & 0 & 0 & 0 \end{bmatrix}, B_3 = \begin{bmatrix} 0 & 0 & 0 & 0 \\ 0 & 0 & 0 & 0 \\ 0 & 0 & 0 & 1 \\ 0 & 0 & 0 & 0 \end{bmatrix},$$

$$B_4 = \begin{bmatrix} 0 & 0 & 0 & 0 \\ 0 & 0 & -1 & 0 \\ 0 & 1 & 0 & 0 \\ 0 & 0 & 0 & 0 \end{bmatrix}, B_5 = \begin{bmatrix} 0 & 0 & 1 & 0 \\ 0 & 0 & 0 & 0 \\ -1 & 0 & 0 & 0 \\ 0 & 0 & 0 & 0 \end{bmatrix}, B_6 = \begin{bmatrix} 0 & -1 & 0 & 0 \\ 1 & 0 & 0 & 0 \\ 0 & 0 & 0 & 0 \\ 0 & 0 & 0 & 0 \end{bmatrix}.$$

The *Sim(3)* adds another degree of scaling to 3D rigid transformations and the generators are the same except for an additional generator:

$$B_7 = \begin{bmatrix} 0 & 0 & 0 & 0 \\ 0 & 0 & 0 & 0 \\ 0 & 0 & 0 & 0 \\ 0 & 0 & 0 & -1 \end{bmatrix}$$

2.4 Ordinary Differential Equations

As seen in Eqn. 2.13 we fashion our homography parameters using a multi-resolution pyramid. But due to successive stages of gaussian blurring, the edges and structures at each level are shifted a bit and hence, it is naive to assume that the same set of parameters can be used for every level. So, we frame this change of parameters from level to level as a dynamic system.

To provide some background, the quintessential example of dynamic systems are systems that are modelled as a function of time. Although it is more common to see them expressed as equations which specify how they change with time rather than specifying the value at a particular time. This leads to them being often expressed as differential equations. A differential equation is an equation which contains a function and one or more of its derivatives. For eg., a first order differential equation is of the form

$$\frac{dy}{dt} = f(y,t) \tag{2.17}$$

To be more specific, in this thesis we deal with the Initial Value Problem, which deals with a particular type of differential equation, called the Ordinary Differential Equation (ODE). An ODE is a differential equation that involves only ordinary derivatives (as opposed to partial derivatives). In the Initial Value Problem, an ODE of this form $\frac{dy}{dt} = f(t,y)$ is known and values in $y(t_0) = y_0$ are known numbers. ODEs can be solved analytically if given in the appropriate form, but normally they are solved numerically. Two of the most common methods of solving them are: Euler's Method [11] and Runge-Kutta 4th Order Method [11].

Euler's method assumes the solution is written in the form of a Taylor Series:

$$y(t+h) = y(t) + hy'(t) + \frac{h^2 y''(t)}{2!} + \frac{h^3 y'''(t)}{3!} + ... \tag{2.18}$$

If we take small values of h, equation 2.18 gives us a reasonably good approximation. For Euler's method, we take just the first two terms only.

$$y_{t+h} = y_t + hf(t,y) \tag{2.19}$$

The Runge-Kutta 4th Order Method is an extension of Euler's method to the fourth order in the Taylor series expansion (Eqn. 2.18). The method is

called a 4th order method because the local truncation error is of the order of $O(h^5)$, while the total accumulated error is order $O(h^4)$.

In the context of this thesis, we parametrize the function f using a neural network. The benefit of doing this with autograd based frameworks is that the parameters of the neural network can be optimized easily and it is trivial to model the dynamics function.

Chapter 3

Related Works

Given that image registration is a fundamental task in image processing pipelines, whether it be for image fusion, remote sensing, organ atlas creation or even tumor growth monitoring, it is an age old problem which has been approached from many angles. Based on the approach used to solve the problem, they can be divided broadly into three categories:

1. Feature based approaches
2. Learning based approaches
3. Optimization based approaches

3.1 Feature based approaches

This family of approaches use "features" which were extracted from the images using various techniques [72]. These features can be point based [3, 9, 17], curves [70, 26, 12] or even a surface model [73] (although point based features are the most prevalent). This extraction involves extracting distinct features from the image which are representative of areas of interest in the image. Quite often in the medical domain, physical markers are also used. These markers can be extrinsic or intrinsic. Extrinsic markers are imprints left by external instruments on the patients area of interest, while intrinsic markers try to use the inherent features of the patients body such as centerline points, curve points, etc. in vessels, arteries, etc. Once these points are obtained, point

set matching algorithms [30] are used to obtain the geometric transformation between the two point sets.

There have been various algorithms proposed for automatic feature extraction in images such as SIFT[46], SURF[6], PCA-SIFT [39], etc. For instance, SIFT works by transforming an image into a collection of feature vectors which are all invariant to translation, rotation, scaling and to some extent illumination changes. Among these, key point descriptors are selected using maxima and minima of the result of difference of gaussians applied to scale space pyramids. Once such a set of feature descriptors is obtained from both images, keypoints representing the same point in both images can be obtained using various clustering methods such as KNN [65]. When using KNN, for each point, the k-closest matches based on a distance metric are computed and using a cut-off criteria, only the best matches are selected. Oftentimes, only those keypoints where the corresponding matched keypoint is significantly closer than the other neighbouring points are kept.

Figure 3.1: Example of feature matching. Source: https://www.sicara.ai/blog/2019-07-16-image-registration-deep-learning

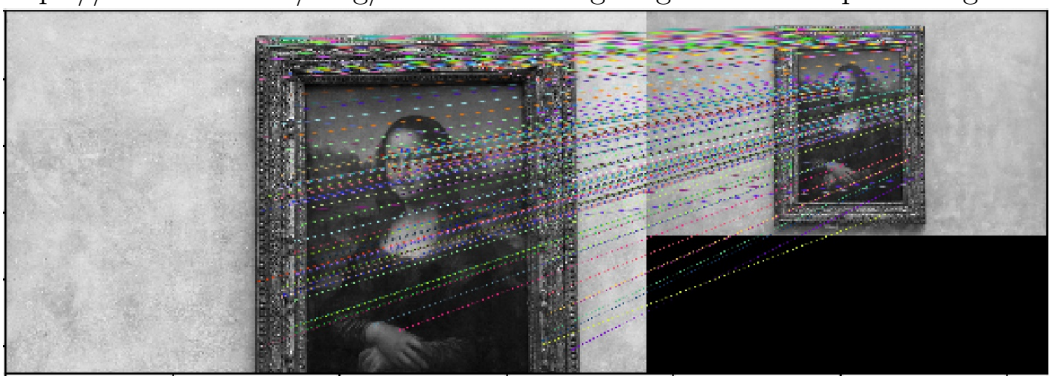

The final step is then to determine the homography transformation matrix from this set of corresponding feature descriptors. RANSAC (Random sample consensus) [23] is then used to sample randomly from this set of good keypoints and compute a homography. Depending on how well this homography matches for rest of the corresponding keypoints in the unsampled set, outliers and inliers are computed for each such randomly sampled set. The homography associated with the smallest number of outliers is selected.

While these methods are quite fast, often the feature detector stage is the bottleneck, so alternative faster feature detectors have been proposed such as Oriented FAST and Rotated BRIEF (ORB) [60] which trade-off time for performance.

- **Pros:** Very fast
- **Cons:** Can be quite inaccurate when:
    1. The feature detector stage performs poorly
    2. There aren't enough detected keypoints
    3. The keypoint matching stage performs poorly due to drastic changes in illumination or large changes in viewing angles

3.2 Learning based approaches

Most learning based approaches are characterized by training a model to learn the transformation between a registered pair of images where the ground truth is available. In recent times, given the prevalence of CNNs as feature extractors, DeTone, Malisiewicz, and Rabinovich [18] proposed homography estimation as a deep learning based supervised learning task. They posit that in a homography matrix, estimating all parameters together is quite a difficult optimization task, since it mixes the rotational and translational terms. They propose to use an alternative four-point parametrization which works better. They create a synthetic dataset using patches from the MS-COCO dataset [45] which have been altered with random homography perturbations in a limited range and use that as the training target.

Cheng, Zhang, and Zheng [15] hypothesize that a similarity metric for multi-modal registration is usually too complex to be represented using intensity based statistical metrics. So they propose learning the similarity metric itself that is trained using a binary classifier to learn the correspondence of two image patches.

- **Pros:** Very fast at inference

Figure 3.2: Structure of HomographyNet as proposed by DeTone, Malisiewicz, and Rabinovich [18]

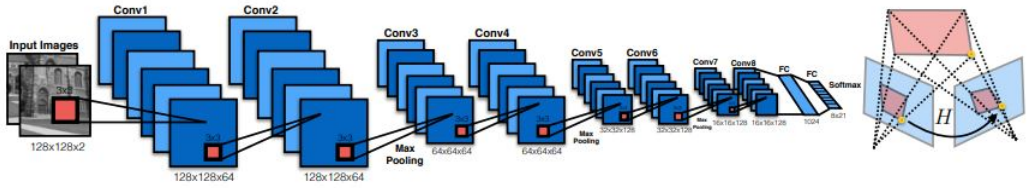

- **Cons:**

    1. Training time for an entire dataset can be quite long.
    2. Needs annotated data.
    3. Performance depends on size of training data available.
    4. Not very robust to data not seen in the training set.

3.3 Optimization based approaches

This thesis primarily deals with ideas in this family of approaches. Optimization based approaches work at the global level by using pixel to pixel matching rather than extracting specialized features and computing descriptors for them. The Lucas-Kanade algorithm [47] is one of the earliest such approaches to doing this. It works by solving the optical flow equations for all the pixels in the neighbourhood my minimizing the mean squares error.

This family of algorithms works by first deciding on a transformation/warping model. This transformation could be deformable or non-deformable. In case of deformable registration, the model is usually parametrized by a displacement vector field and in case of non-deformable registration, the model is paramtrized by a homography matrix. In this work we focus on non-deformable registration transformations. The transformation model is often initialized with a guess and a distance metric is used to compute the quality of the current registration. Often a differentiable metric is preferred because gradient descent based techniques for optimization work quite well to minimize such a cost function as compared to search based optimization. A very intuitive

example of such a cost function is MSE (Mean Square Error) [4]. Often in deformable registration, a weighted regularization term is added to the cost function to enforce constraints, for eg. smoothness of displacement fields.

Since the transformation model focused on this work is homography based, we look at it in more detail. The transformation parameters for the homography matrix are often not optimized directly, but rather alternative methods have been found to have better results. For instance, DeTone, Malisiewicz, and Rabinovich [18] used a four-point parametrization approach. On the other hand, Wachinger and Navab [80] parametrize 3D transformations using matrix exponentials.

There have been attempts to improve the robustness of global optimization based approaches by combining feature based methods [86] or proposing different loss functions such as ECC (Enhanced Correlation Coefficient) [22] or by representing images in the Fourier domain [48].

Nguyen et al. [55] proposed an unsupervised alternative, where they try to use a four-point paramterization as well and use the L1 pixel-wise photometric loss. There have been attempts to speed up optimization by using techniques such as Gaussian pyramids (Section 2.2) or by improving optimization techniques [53], which by themselves are an active area of research.

Given a univariate function $f(w)$, the second order Taylor expansion of f around an initial point w_0 is:

$$f(w) \approx f(w_0) + (w - w_0)f'(w_0) + \frac{1}{2}(w - w_0)^2 f''(w_0) \tag{3.1}$$

A stationary point of this $f(w)$ can be found by setting its first derivative to 0, i.e.:

$$f'(w) \approx f'(w_0) + (w - w_0)f''(w_0) = 0 \tag{3.2}$$

Solving this we can get:

$$w_1 = w_0 - \frac{f'(w_0)}{f''(w_0)} \tag{3.3}$$

Performing this update in an iterative manner, we get the general equation:

$$w_{t+1} = w_t - \frac{f'(w_t)}{f''(w_t)} \tag{3.4}$$

This is called Newton's method of optimization or second-order gradient descent. Depending on the number of terms used from Eqn. 3.1 we can also have first-order gradient descent methods if we ignore the final second-order term. This leads to more inaccurate but faster updates. The Levenberg–Marquardt [44] algorithm is another such optimization technique which has been used for solving non-linear least squares problems. In a multi-variate setting, computing the inverse of the second order term in Eqn. 3.4 becomes a very expensive and slow process, hence, a third family of optimization techniques exist called *Quasi-Newton* methods, which use an approximation of the inverse of the second order term.

- **Pros:**
    1. Needs no annotated training data.
    2. Works for any pairwise registration task given a suitable cost function
- **Cons:**
    1. Slower as compared to other approaches (at inference time)

Chapter 4

Proposed Multi-Resolution Image Registration

In this section, we present two algorithms: DRMIME and ODECME. The first, DRMIME, brings in the ideas of using MINE as a loss function and using Matrix Exponential for parametrization. The second, ODECME, builds on these ideas and further refines the algorithm by adding complex matrix exponentials, ODEnet and a symmetric loss function.

4.1 Differentiable Mutual Information and Matrix Exponential for Multi-Resolution Image Registration

4.1.1 MINE for images

While MINE is a general purpose estimator for MI between any two n-dimensional variables, we adapt it slightly as below (Algorithm 1) to use it for pairwise image MI computation. Our objective as proposed in Eqn. 2.1 now becomes (MI needs to be maximised for registration):

$$\max_{v_1,v_2,\ldots} MINE(T, Warp(M, Mexp(\sum_i v_i B_i))). \tag{4.1}$$

Algorithm 1 takes in two images X and Z along with a subset of pixel locations I. It creates a random permutation I^s of the indices I. I_j denotes the j^{th} entry in the index list I, while X_{I_j} denotes the I_j^{th} pixel location on

Algorithm 1: MINE

$MINE(X, Z, I)$
Input: Image X, Image Z, Sampled pixel locations I
Output: Estimated mutual information (DV lower bound)
Shuffle pixel locations: $I^s = RandomPermute(I)$;
$N = length(I)$;
$DV = \frac{1}{N}\sum_j f_\theta(X_{I_j}, Z_{I_j}) - log(\frac{1}{N}\sum_j exp(f_\theta(X_{I_j}, Z_{I_j^s})))$;
Return DV;

image X. Finally, the algorithm returns the DV lower bound [8] computed by Monte Carlo approximation of (2.11).

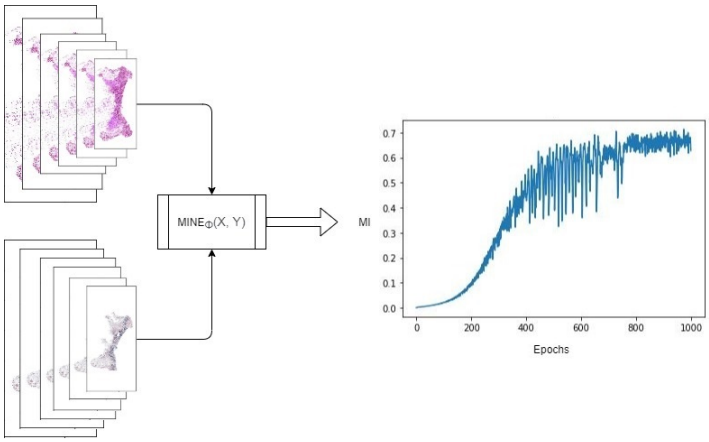

Figure 4.1: Given a pair of images, MINE converges to the DV lower bound.

Using a multi-resolution approach, the cost function (Eqn. 4.1) becomes:

$$\max_{v_1,...,v_6} \sum_{l=1}^{L} MINE(T_l, Warp(M_l, Mexp(\sum_{i=1}^{6} v_i B_i))). \tag{4.2}$$

However, note also that image structures are slightly shifted through multi-resolution image pyramids. So, a transformation matrix suitable for a coarse resolution may need a slight correction when used for a finer resolution. To mitigate this issue, we exploit matrix exponential parameterization and introduce an additional parameter vector $v^1 = [v_1^1, ..., v_6^1]$ exclusively for the finest resolution and modify optimization (4.2) as follows:

$$\max_{\substack{v_1,\cdots,v_6 \\ v_1^1,\cdots,v_6^1 \\ \theta}} \{\sum_{l=2}^{L} MINE(T_l, Warp(M_l, Mexp(\sum_{i=1}^{6} v_i B_i))) + MINE(T_1, Warp(M_1, Mexp(\sum_{i=1}^{6} (v_i + v_i^1) B_i)) \tag{4.3}$$

where θ denotes the parameters of the neural network that MINE uses to realize f.

4.1.2 DRMIME Algorithm

Fig. 4.2 shows a schematic for the optimization problem (4.3). Our proposed algorithm DRMIME (Algorithm 2) implements DRMIME [54] that uses DV lower bound (2.11) computed in turn by Algorithm 1, which employs a fully connected neural network f_θ MINEnet. MINEnet has two hidden layers with 100 neurons in each layer. We use ReLU non-linearity in both the hidden layers. The Appendix contains details about other hyperparameters. The code for DRMIME is available here.

Algorithm 2: DRMIME

Input: Fixed image T, moving image M
Output: Transformation matrix H_1
Set learning rates α, β, γ and pyramid level L;
Build multiresolution image pyramids $\{T_l\}_{l=1}^{L}$ from T and $\{M_l\}_{l=1}^{L}$ from M;
Use random initialization for MINEnet parameters θ ;
Initialize v and v^1 to the 0 vectors ;
for *each iteration* **do**
    $MI = 0$;
    $H = Mexp(\sum_{i=1}^{6} v_i B_i)$;
    $H_1 = Mexp(\sum_{i=1}^{6} (v_i + v_i^1) B_i)$;
    $I_1 =$ Sample pixel locations on T_1 ;
    $MI += MINE(T_1, Warp(M_1, H_1), I_1)$;
    for $l = [2, L]$ **do**
        $I_l =$ Sample pixel locations on T_l ;
        $MI += MINE(T_l, Warp(M_l, H), I_l)$;
    end
    Update MINEnet parameter: $\theta += \alpha \nabla_\theta MI$;
    Update matrix exponential parameters: $v += \beta \nabla_v MI$ and $v^1 += \gamma \nabla_{v^1} MI$;
end
Compute final transformation matrix: $H_1 = Mexp(\sum_{i=1}^{6} (v_i + v_i^1) B_i)$;

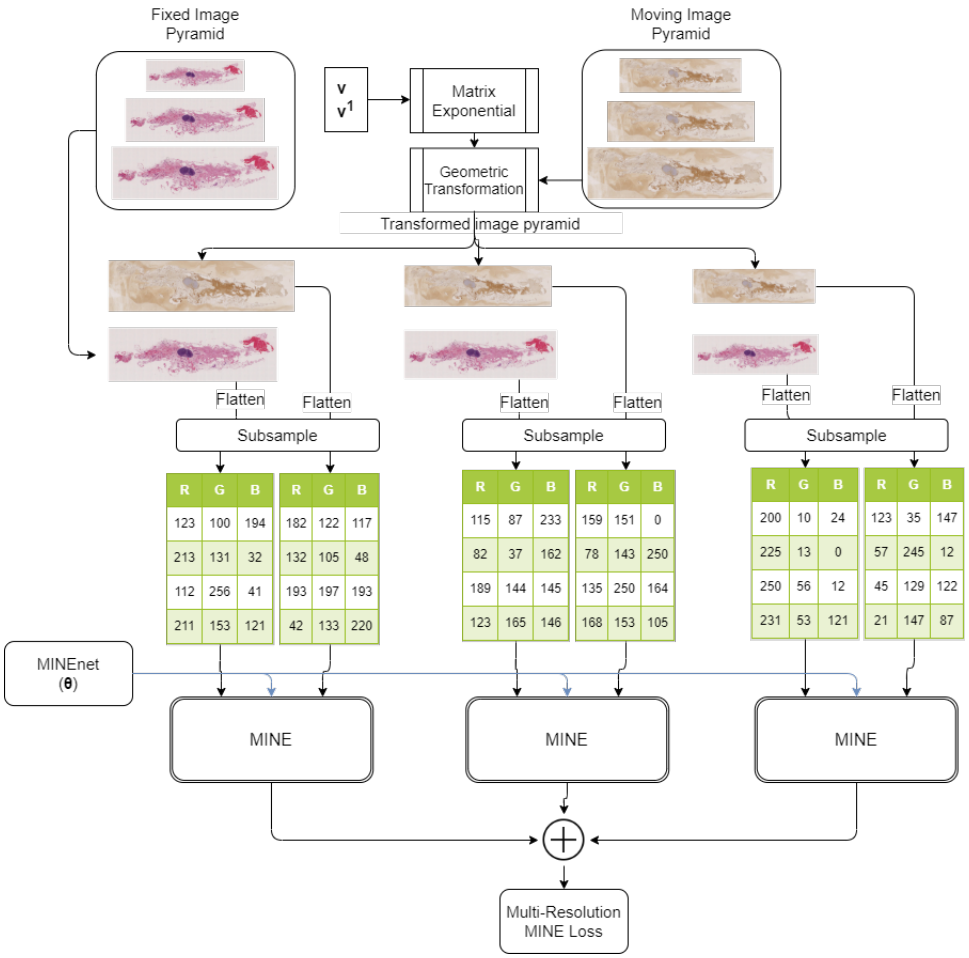

Figure 4.2: Pipeline for the DRMIME Registration algorithm

Algorithm 2 builds two image pyramids, one for the fixed image T and another for the moving image M. Due to memory constraints, especially for GPU, a few pixel locations are sampled that enter actual computations. This step appears as "Subsample" in Fig. 4.2. We have used two variations of sampling: (a) randomly choosing only 10% of pixels locations on each resolution and (b) finding Canny edges [13] on the fixed image and choosing only the edge pixels. Our ablation study shows a comparison between these two options. Fig. 4.2 illustrates two other computation modules- "Matrix Exponential" and "Geometric Transformation" that denote $Mexp$ and $Warp$ operations, respectively.

4.2 Ordinary Differential Equation and Complex Matrix Exponential for Multi-resolution Image Registration

With DRMIME, we notice that we use the same parameters for all multi-resolution levels except the last. The intuition still remains that all levels need some additional changes from the previous level, which implies that all levels ideally have their own coefficients and the change from one level to the next is related in some manner. We can model the dynamics of these changes to improve performance of the registration algorithm. Furthermore, due to the surjectivity of the real valued matrix exponential many geometric transformation matrices in the vector space cannot be reached and this could potentially hurt performance. We remedy this by using complex matrix exponential.

4.2.1 ODE for Multi-resolution Image Registration

Image structures are slightly shifted through multi-resolution Gaussian image pyramids [82]. So, a transformation matrix suitable for a coarse resolution may need a slight correction when used for a finer resolution. To mitigate this issue, we model matrix exponential parameters as a continuous function $v(s)$ of resolution s. The change in $v(s)$ over resolution s can be modeled by a neural network g_ϕ with parameters ϕ:

$$\frac{dv(s)}{ds} = g_\phi(s, v(s)). \tag{4.4}$$

The added benefit of using a neural network as the function g is that neural networks are differentiable and hence, using the autograd feature of modern packages (e.g., PyTorch, Tensorflow) we can easily compute derivatives for updating the parameters of the neural network.

Using Euler method [11] the ordinary differential equation (ODE) (4.4) can be solved for all resolution levels $1, 2, ..., L$:

$$\begin{aligned} v_L &= u \\ \text{for } l &= L-1, L-2, \cdots, 1 \\ v_l &= v_{l+1} + (s_l - s_{l+1}) g_\phi(s_{l+1}, v_{l+1}), \end{aligned} \tag{4.5}$$

where $v_l = [v_{l,1}, v_{l,2}, ...]$ are the matrix exponential coefficients for resolution level l and $s_l = d^{-l+1},\ l = 1, 2, .., L$ denote the discrete resolutions in powers of the downscale factor d. $u = [u_1, u_2, ...]$ is the initial value vector in the ODE and it is an optimizable parameter of the model along with the neural network parameters ϕ. We have also used 4-point Runge-Kutta method (RK4) [11] for the above recursion:

$$\begin{aligned} v_L &= u \\ \text{for } l &= L-1, L-2, \cdots, 1 \\ h &= s_l - s_{l+1}, \\ k_1 &= h g_\phi(s_{l+1}, v_{l+1}), \\ k_2 &= h g_\phi(s_{l+1} + \tfrac{1}{3}h, v_{l+1} + \tfrac{1}{3}k_1), \\ k_3 &= h g_\phi(s_{l+1} + \tfrac{2}{3}h, v_{l+1} - \tfrac{1}{3}k_1 + k_2), \\ k_4 &= h g_\phi(s_l, v_{l+1} + k_1 - k_2 + k_3), \\ v_l &= v_{l+1} + \tfrac{1}{8}(k_1 + 3k_2 + 3k_3 + k_4). \end{aligned} \tag{4.6}$$

Generating matrix exponential coefficients $v_l,\ l = 1, 2, .., L$ by the ODE solution (4.5) or (4.6), the optimization for image registration (4.9) using mutual information now becomes:

$$\begin{aligned} \max_{\substack{u_1,u_2,\cdots \\ \phi,\theta}} \sum_{l=1}^{L} \{ & MINE(T_l, Warp(M_l, Mexp(\sum_i v_{l,i} B_i))) + \\ & MINE(M_l, Warp(T_l, Mexp(-\sum_i v_{l,i} B_i)))\}. \end{aligned} \tag{4.7}$$

4.2.2 Symmetric loss function

Usually in image registration tasks, only the moving image is transformed and then a cost function is used to compute the *distance* metric between the fixed image and the transformed moving image. Given the entire multi-resolution pyramid the cost function (Eqn. 4.1) is then:

$$\min_{v_1,v_2,\cdots} \sum_{l=1}^{L} \{ D(T_l, Warp(M_l, Mexp(\sum_i v_i B_i))) \tag{4.8}$$

Since we use matrix exponential coefficients to parametrize our transform, it is very simple to compute the inverse transform and apply it to the moving image. Computing the inverse is as straightforward as:

$$H^{-1} = Mexp(-\sum_i v_i B_i)$$

This way we add an additional term to our cost function, which is the cost of registering the fixed image to the moving image as well.

$$\begin{aligned}\min_{v_1,v_2,\ldots} \sum_{l=1}^{L} \{ & D(T_l, Warp(M_l, Mexp(\sum_i v_i B_i))) + \\ & D(M_l, Warp(T_l, Mexp(-\sum_i v_i B_i)))\},\end{aligned} \tag{4.9}$$

This alters our objective of registering one moving image to a fixed image and changes it to an objective where we register the images to each other mutually. This symmetric cost function is likely to help make the registration much more robust since the geometric transform and its inverse both need to be correct simultaneously, but also at the same time they remain parametrized by common parameters which are optimized at the same time.

4.2.3 Complex Matrix Exponential

It is well known that exponential of real valued matrix is not globally surjective, i.e., not all transformation matrices (affine or homography) can be obtained by the exponential of real-valued matrices [24]. One way to overcome this issue is to compose matrix exponential a few times to compute the transformation matrix.

In this work, we propose to use complex matrix exponential an alternative to the scheme using composition, because complex matrix exponential is globally surjective [24]. Thus, a complex matrix, $B^r + \sqrt{-1}B^i = \sum_i v_i B_i$, produced by complex parameters, $v_i = v_i^r + \sqrt{-1}v_i^i$, can use matrix exponential series (2.15) to create a complex transformation matrix,

$$H^r + \sqrt{-1}H^i = Mexp(B^r + \sqrt{-1}B^i). \tag{4.10}$$

Next, we choose to transform a point (x, y) to another point (x', y') using the following:

$$\begin{aligned}[x^r, y^r, z^r]^T = H^r[x, y, 1]^T,\ [x^i, y^i, z^i]^T = H^i[x, y, 1]^T, \\ x' = \frac{x^r z^r + x^i z^i}{(z^r)^2 + (z^i)^2},\ y' = \frac{y^r z^r + y^i z^i}{(z^r)^2 + (z^i)^2}.\end{aligned} \tag{4.11}$$

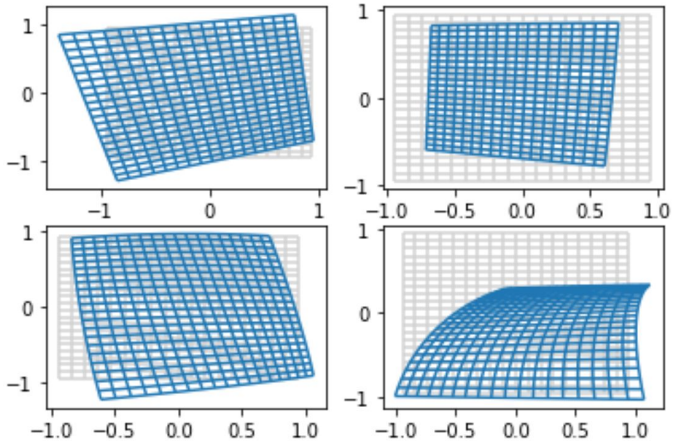

Figure 4.3: Randomly generated grids by complex matrix exponential (4.10) and complex transformation (4.11). Elements of B^r were generated by a zero mean Gaussian with 0.1 standard deviation (SD) for all four panels. Elements of B^i were generated by a zero mean Gaussian with SD as follows: 0 for top-left, 0.1 for top-right, 0.2 for bottom-left and 0.3 for bottom-right panel.

Note that under our chosen transformation (4.11) the straight lines are not guaranteed to remain straight. However, if $H^i = 0$, transformation (4.11) degenerates to a linear transformation using homogeneous coordinates. Fig. 4.3 shows four randomly generated grids using (4.10) and (4.11). When imaginary coefficients are zeros (top-left panel, where $B^i = 0$ and consequently $H^i = 0$), the transformation acts as a homography, whereas the degree of the non-linearity in the transformation increases as the magnitude of B^i increases. Unlike, a 2D Mobius transformation [40], the proposed complex transformation does not guarantee self-intersection. However, note that 2D Mobius transformation is more restrictive, as for example, it cannot generate a perspective transformation.

4.2.4 ODECME Algorithm

Combining the aforementioned elements, ordinary differential equation (ODE) (Section 4.2.1) and complex matrix exponential (CME) (Section 4.2.3), our proposed Algorithm 3 (ODECME) first builds two image pyramids, one for the fixed and another for the moving image. It then computes Euler recursion for ODE-based computation of CME coefficients. Alternatively, we have also

used RK4 recursion (4.6) in our experiments. Note also that "Mexp" may refer to real or complex matrix exponential, depending on whether u and v_l are complex or real. Also, "MINE" can be replaced by any differentiable loss for image registration. "MINEnet" in Algorithm 3 denotes f_θ, (refer to (2)) which is a fully connected neural network [54]. "ODEnet" refers to the fully connected neural network g_ϕ appearing in (4.5) and (4.6). Taking advantage of matrix exponential, we use symmetric loss, which uses both the forward and the inverse transformation matrices. For any gradient computation, such as $\nabla_\theta MI$ or $\nabla_\phi MI$, we use autograd (bult-in optimizers) of PyTorch [56]. Algorithm 3 finally outputs original resolution transformation matrix and its inverse.

Figure 4.4: Pipeline for the ODECME Registration algorithm (using multi-resolution pyramid of 3 levels)

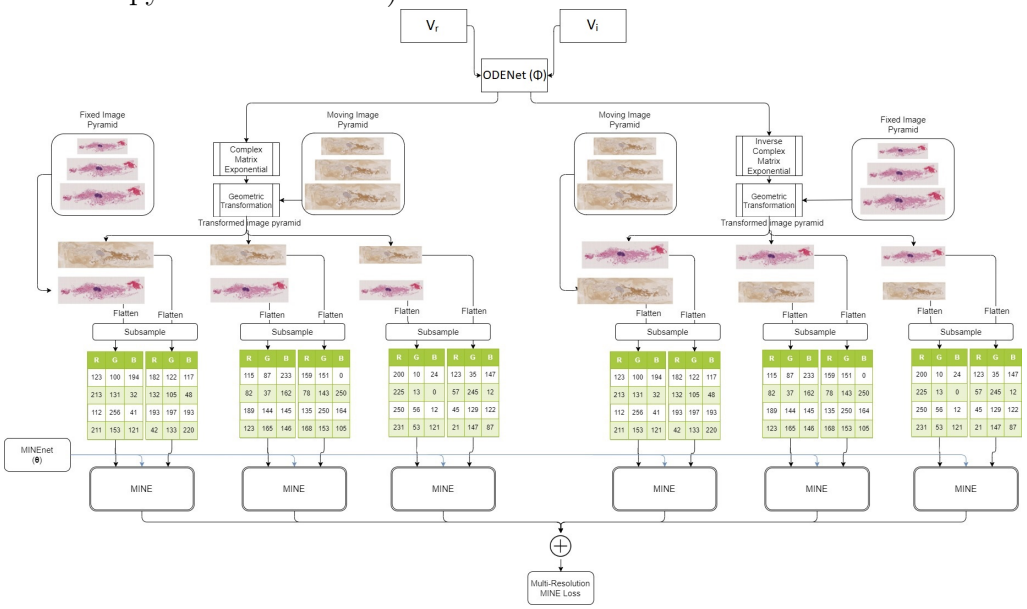

Algorithm 3: ODECME

Build multiresolution image pyramids $\{T_l, M_l\}_{l=1}^{L}$;
Set learning rates α, β and γ;
Use random initialization for MINEnet parameters θ ODEnet parameters ϕ ;
Initialize u to the 0 vector ;
for *each iteration* **do**
  $v_L = u$;
  $H_L = Mexp(\sum_i v_{L,i} B_i)$;
  $H_L^{-1} = Mexp(-\sum_i v_{L,i} B_i)$;
  for $l = [L-1, .., 1]$ **do**
    $v_l = v_{l+1} + (s_l - s_{l+1}) f_\phi(s_{l+1}, v_{l+1})$;
    $H_l = Mexp(\sum_i v_{l,i} B_i)$;
    $H_l^{-1} = Mexp(-\sum_i v_{l,i} B_i)$;
  end
  $MI = 0$;
  for $l = [1, L]$ **do**
    $MI+ = MINE(T_l, Warp(M_l, H_l))$;
    $MI+ = MINE(M_l, Warp(T_l, H_l^{-1}))$;
  end
  Update MINEnet parameter: $\theta+ = \alpha \nabla_\theta MI$;
  Update ODEnet parameter: $\phi+ = \beta \nabla_\phi MI$;
  Update matrix exponential parameter: $u+ = \gamma \nabla_u MI$;
end
Compute final transformation matrices:
$v_L = u$;
for $l = [L-1, .., 1]$ **do**
  $v_l = v_{l+1} + (s_l - s_{l+1}) f_\phi(s_{l+1}, v_{l+1})$;
end
$H_1 = Mexp(\sum_i v_{1,i} B_i)$;
$H_1^{-1} = Mexp(-\sum_i v_{1,i} B_i)$;

Chapter 5

Experiments

5.1 Datasets

The datasets chosen for our experiments correspond to testing two important hypotheses. First, performing image registration with our algorithm on images within the same modality fares comparably (or better) to other standard algorithms. For this, we use the FIRE (Fundus Image Registration) dataset [31]. Second, since our algorithm is based on MI, it can handle multi-modal registration successfully as well. For this we use data from the ANHIR (Automatic Non-rigid Histological Image Registration) 2019 challenge[10].

Furthermore, since Mutual Information can be used even for volumetric data, we applied our algorithm to the IXI (Information eXtraction from Images) dataset [1] for testing mono-modal registration performance and the ADNI (Alzheimer's Disease Neuroimaging Initiative) dataset [85] for multi-modal registration.

5.1.1 FIRE

The FIRE dataset consists of 134 retinal fundus image pairs. These pairs are classified into three categories depending on what purpose they were collected for: S (Super resolution, 71 pairs), P (Mosaicing, 49 pairs) and A (Longitudinal Study, 14 pairs). Of these, Category P pairs have $< 75\%$ overlap which provides a near impossible challenge for gradient based algorithms, not just ours, but also for the competing algorithms. The registration optimization

[1] IXI dataset: https://brain-development.org/ixi-dataset/

even diverges in a lot of cases, and hence we leave out this subset of images in our experiments and use only Categories S and A.

Figure 5.1: Pairs in each column belong to the same category. Column categories from left to right: S, P, A, A. White dots indicate control point locations. Source: https://projects.ics.forth.gr/cvrl/fire/

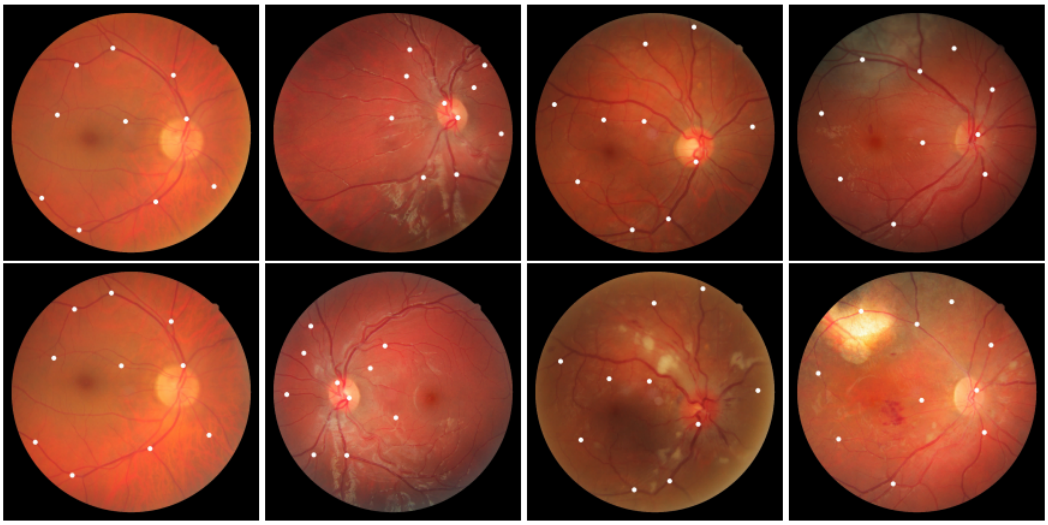

Ground Truth

The FIRE dataset provides ground truth in the form of coordinates of 10 corresponding control points between the fixed and the moving image. These points were chosen manually by experts and further refined using computational methods.

Preprocessing

Also, while the images are square in shape, the retinal fundus is circular in shape and hence the gap between the edges of the fundus and the image border is quite large and is completely black. This leads to erroneous metrics when measuring loss functions such as MSE or MI over the entire image. So, we crop the central portion of the image to only include the fundus and final size of the cropped image is 1941×1941 pixels.

Evaluation

For evaluating registration accuracy, we compute the Euclidean distance between these corresponding points after registration and average them. Also the image coordinates are scaled to be between 0 and 1 so that images of different sizes can be compared using the same benchmark. We call this measure the Normalized Average Euclidean Distance (NAED). Most competing methods do not support a homography based registration model, so an affine model was used to be consistent all across.

5.1.2 ANHIR

The ANHIR (Automatic Non-rigid Histological Image Registration) dataset provides high-resolution histopathological tissue images stained with different dyes. This provides a multi-modal challenge.

Figure 5.2: Different types of samples in ANHIR. Source: https://anhir.grand-challenge.org/

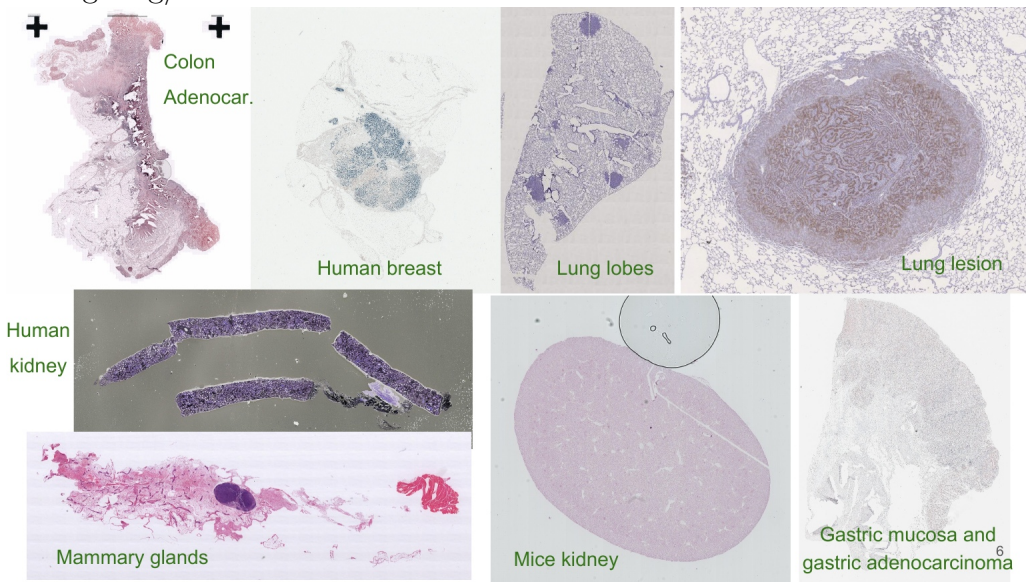

Ground Truth

The ground truth provided is similar to the FIRE dataset, except for the fact that more than 10 corresponding coordinates might be provided as the ground

truth in certain pairs. Also, we use only the training set provided in the database, since only those pairs (230) have the ground truth available.

Preprocessing

The ANHIR dataset has some incredibly large resolution images (upto $100k \times 200k$ pixels). Some of the competing registration frameworks were unable to process such large images and so, we downscaled every image by a factor of 5 to make them available to every framework. Furthermore, each staining can have a different resolution as well, so the fixed and moving image pairs need not be the same size. So, to remedy this, we rescale the image with a smaller aspect ratio to match the width of the paired image. Post that the height is padded to match the other image as well. This preprocessing is consistent across all algorithms and allows us to maintain the aspect ratios of the individual images and have both images in a pair at the same resolution without any distortions.

Evaluation

We use NAED as the evaluation metric here as well and use an affine model for transformation.

5.1.3 IXI

The IXI dataset has about 600 MR images from healthy patients. It includes T1, T2, PD-weighted images, MRA images, and Diffusion-weighted images.

Preprocessing

We choose 51 T1 volumes (at random) which have the same size and designate one as the Atlas (reference volume) and register the other 50 volumes against it. All the voxel intensity values were normalised.

Evaluation

Unfortunately, the IXI dataset does not come with any form of ground truth, so we resort to standard measures [28] for registration accuracy such as SSIM[64], PSNR[63] and SSD (Sum of Squared Differences). The SSIM, PSNR, SSD

scores are computed after every registration with the Atlas and averaged and then reported for each algorithm. The transformation model used has 7 degrees of freedom, composed of isotropic scaling with three axes of rigid transformation and three axes for rotation.

5.1.4 ADNI

The ADNI dataset provides 1.5T and 3T MRI scans of patients scanned over different periods of time.

Preprocessing

We chose one volume as the atlas (reference volume) from the ADNI1:Screening 1.5T collection and another 50 volumes from the ADNI1:Baseline 3T collection. All voxel intensity values were normalized, and resized to match the reference volume ($160 \times 192 \times 192$) before feeding into any of the algorithms.

Evaluation

Similar to the IXI dataset, no groundtruth is available here too, so we report the averaged SSIM and PSNR metrics for the dataset after registration. The transformation model used has 7 degrees of freedom, composed of isotropic scaling with three axes of rigid transformation and three axes for rotation.

5.2 Competing algorithms

We evaluate our method against the following off-the-shelf registration algorithms from popular registration frameworks. The competing algorithms were whether they use MI or can be used for multi-modal registration:

1. **Mattes Mutual Information (MMI)** [50, 51, 36]: As mentioned in equation (2.6), we need to compute the joint and marginal probabilities of the fixed and moving images. To reduce the effects of quantization from interpolation and discretization due to binning, this version of MI computation uses Parzen windowing to form continuous estimates of the underlying image histogram.

2. **Joint Histogram Mutual Information (JHMI)** [76, 35]: This method computes Mutual Information using Parzen windows as well, but it uses separable Parzen windows. By selection of a Parzen window that satisfies the partition of unity, it provides a tractable closed-form expression of the gradient of the MI computation with respect to transformation parameters.

3. **Normalized Cross Correlation (NCC)**[38]: As the names says, the correlation between the moving and the fixed image pixel intensities is computed. The correlation is normalized by the autocorrelations of both the fixed and moving images.

4. **Mean Square Error (MSE)**[37]: This is the mean squared difference of the pixelwise intensity between the fixed and moving image.

5. **AirLab Mutual Information (AMI)**[61]: AirLab is a PyTorch based image registration framework. It performs histogram based mutual information computation[79, 49]. Since it is a deep learning based solution, it provides support for using batches as well as state-of-the-art optimizers and GPU support.

6. **Normalized Mutual Information (NMI)**[68, 41]: The initial PDF (probability density function) construction is done using Parzen histograms, and then MI is obtained by double summing over the discrete PDF values. In this metric, the final MI is normalized to a range between 0 and 1.

Also as a note, most libraries limit 2D image registration to affine transforms in terms of degrees of freedom. While it is possible to use perspective transforms with our algorithm just by changing the base vector (v), in order to have a fair comparison, we limit our algorithm to affine transforms as well.

In case of 3D volume registration, since the highest degree of freedom for geometric transforms supported for 3D volumes is the similarity transform, that is what we use for comparison. It consists of a rotation, translation and

isotropic scaling to the space. The implementations of the above algorithms were used from these packages:

- SITK[67]: MMI, JHMI, NCC, MSE
- AirLab[1]: AMI
- SimpleElastix[66]: NMI

In terms of sampling, we noticed using Canny edge-detection based sampling helps registration results slightly. In the following results, the DRMIME algorithm uses Canny sampling. We look at its effects in the ablation study (Section 5.4.3). Since other frameworks don't have access to such a pre-processing step in their pipeline, to ensure a fair comparision between them and ODECME, we use random sampling, the hyperparameters for which are in the Appendix (Section A.2).

5.3 Results

This section lists the results for all algorithms on the aforementioned datasets. For all evaluations, we also conduct a paired t-test with DRMIME (with real matrix exponential) to investigate if the results are statistically significant (p-value < 0.05). These p-values show that the changes brought in by DRMIME were statistically significant (or not) compared to other algorithms available in registration toolboxes; and also if elements added by ODECME led to results statistically significantly different to DRMIME. Please note, unless explicitly mentioned, DRMIME refers to the vanilla version of DRMIME which uses just real matrix exponential.

Fig. 5.3 shows registration results for a random FIRE sample. Table 5.1 shows the NAED for all algorithms on the FIRE dataset. Here, DRMIME/ODECME performs almost an order of magnitude better than the competing algorithms and the results are statistically significant.

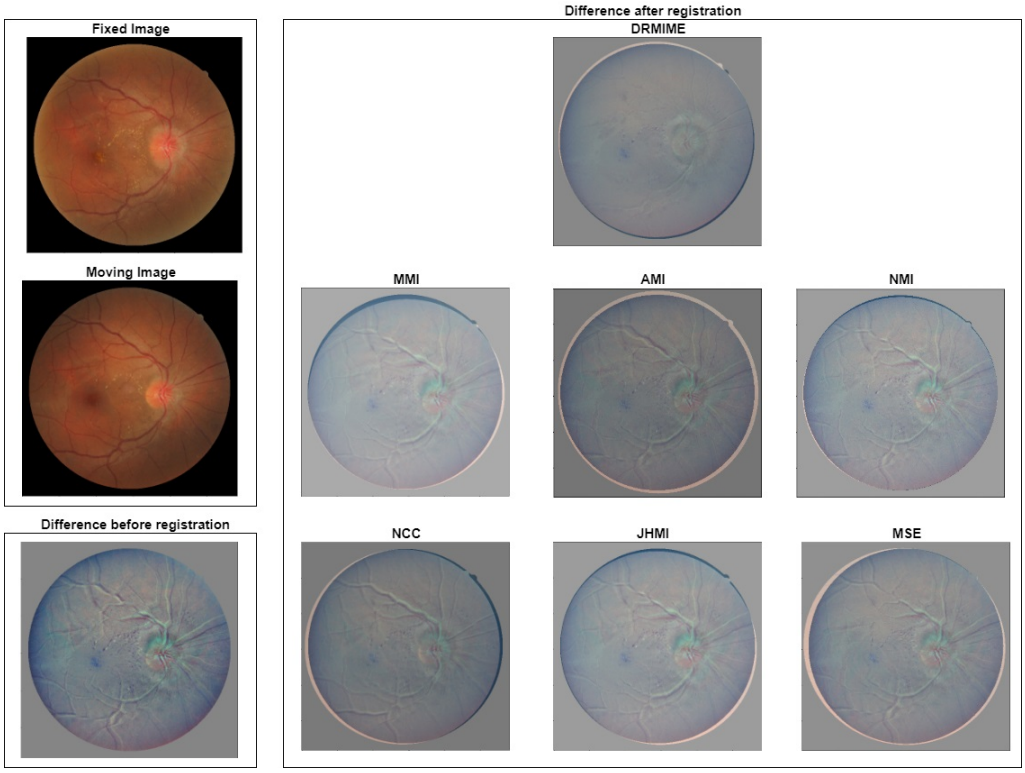

Figure 5.3: The images on the left show a pair to be registered from the FIRE dataset. The images on the right represent the difference between the transformed moving image and the fixed image after registration by different algorithms. Source: Nan et al. [54]

Table 5.1: NAED for FIRE dataset along with paired t-test significance values

Algorithm	NAED (Mean ± STD)	p-value
ODE (RK4-Complex)	**0.00381** ± 0.010	0.0032
ODE (RK4-Real)	0.00385 ± 0.014	0.0032
DRMIME (Complex)	0.00482 ± 0.031	0.1021
DRMIME (Real)	0.00482 ± 0.014	-
ODE (Euler-Complex)	0.0049 ± 0.016	0.0822
ODE (Euler-Real)	0.0049 ± 0.016	0.1053
NCC	0.0194 ± 0.033	1.3e-04
MMI	0.0198 ± 0.034	5.4e-05
NMI	0.0228 ± 0.032	1.7e-08
JHMI	0.0311 ± 0.046	4.5e-07
AMI	0.0441 ± 0.028	1.4e-27
MSE	0.0641 ± 0.094	3.5e-03

Fig. 5.4 presents a closer look at the same metrics from Table 5.1. We note

that ODECME has very few outliers due to the robustness of the algorithm. Also as another note, in this and the following box plots, we present the best version of the DRMIME/ODECME (i.e. ODE (RK4-Complex)) as ODECME algorithm since they belong to the same family of algorithms and we want to present their utility in contrast to other algorithms.

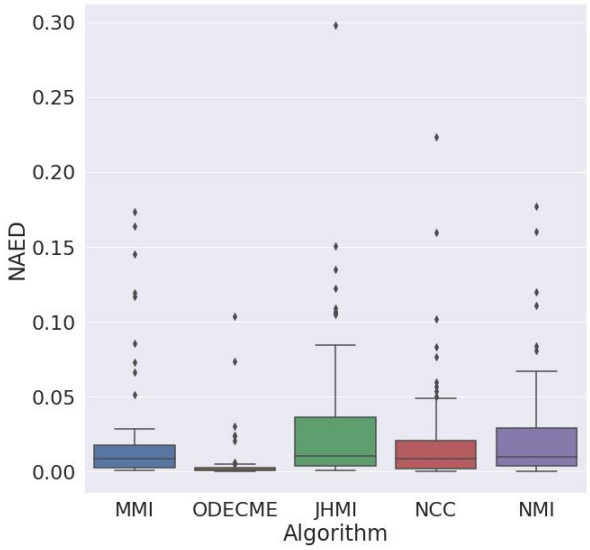

Figure 5.4: Box plot for NAED of the best 5 performing algorithms on FIRE. ODECME refers to ODE (RK4-Complex).

Fig. 5.5 shows registration results for a random sample from ANHIR. Table 5.2 presents the NAED metrics for the ANHIR dataset. While the margin of improvement is not as large as in case of the FIRE dataset, DRMIME/ODECME is still statistically the best performing algorithm.

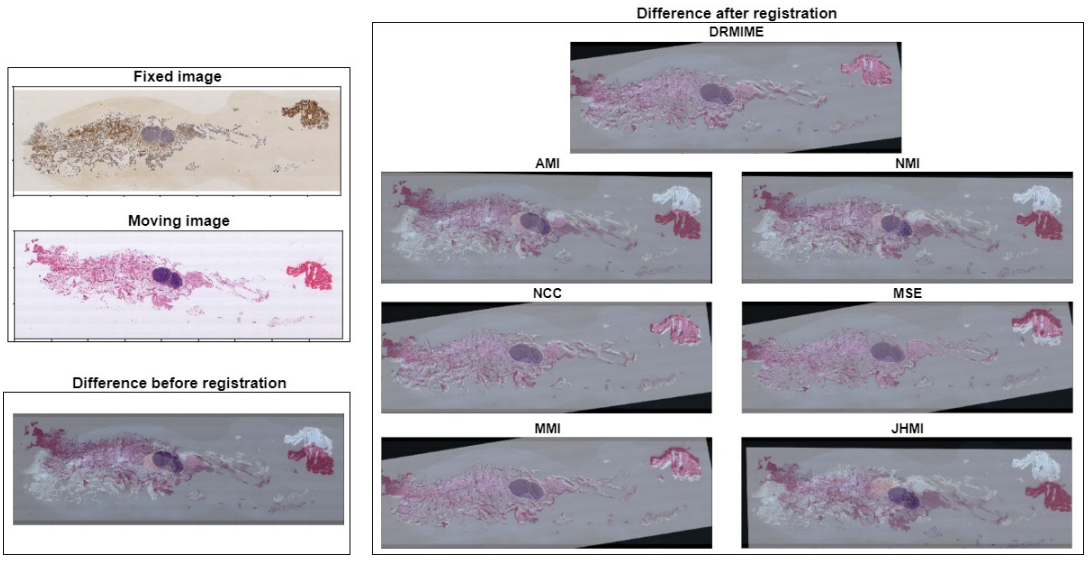

Figure 5.5: The images on the left show a pair to be registered from the ANHIR dataset. The images on the right represent the difference between the transformed moving image and the fixed image after registration by different algorithms.

Table 5.2: NAED for ANHIR dataset along with paired t-test significance values

Algorithm	NAED (Mean ± STD)	p-value
ODE (RK4-Complex)	**0.0345** ± 0.050	0.0441
ODE (RK4-Real)	0.0348 ± 0.044	0.0642
ODE (Euler-Complex)	0.0361 ± 0.084	1.0e-03
ODE (Euler-Real)	0.0391 ± 0.035	1.5e-03
DRMIME (Real)	0.0384 ± 0.087	-
DRMIME (Complex)	0.0373 ± 0.021	0.0619
NCC	0.0461 ± 0.084	7.0e-04
MMI	0.0490 ± 0.082	6.2e-05
MSE	0.0641 ± 0.094	5.5e-14
NMI	0.0765 ± 0.090	3.0e-31
AMI	0.0769 ± 0.090	3.7e-30
JHMI	0.0827 ± 0.100	8.3e-21

The box-plots in Fig. 5.6 also emphasise the same conclusion as we saw before, i.e. ODECME outperforms the other competing algorithms.

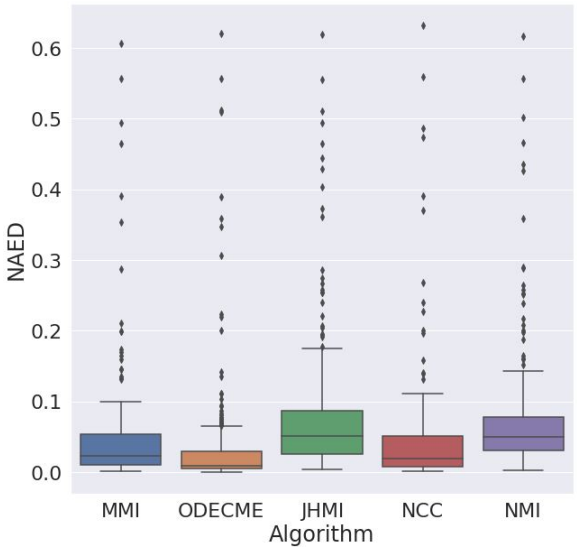

Figure 5.6: Box plot for top 5 performing algorithms on ANHIR. ODECME refers to ODE (RK4-Complex).

For results on the IXI dataset, we compute the SSIM, PSNR and MSE score after registration and present them in Fig. 5.7, 5.8, 5.9 respectively.

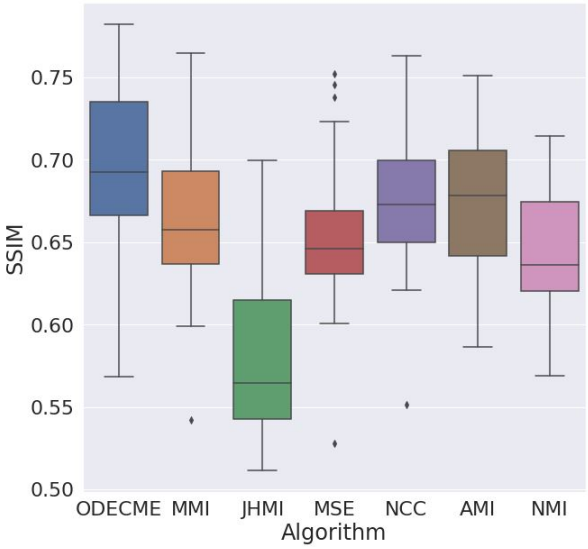

Figure 5.7: Box plot for SSIM values (higher is better) for each algorithm on the IXI datset after registration. ODECME refers to ODE (RK4-Complex).

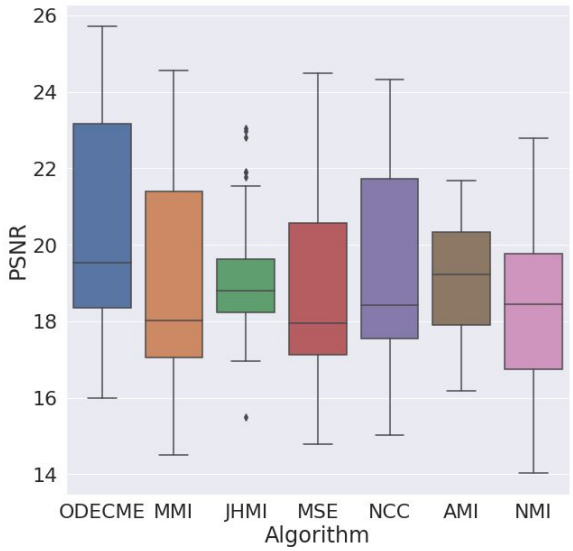

Figure 5.8: Box plot for PSNR values (higher is better) for each algorithm on the IXI datset after registration. ODECME refers to ODE (RK4-Complex).

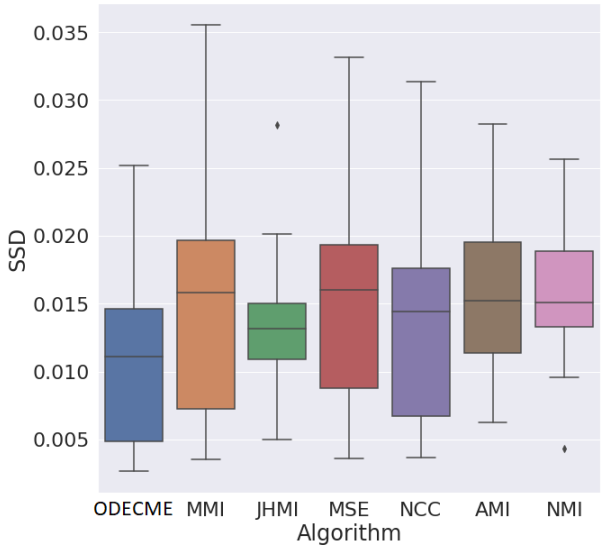

Figure 5.9: Box plot for MSE values (lower is better) for each algorithm on the IXI datset after registration. ODECME refers to ODE (RK4-Complex).

Figure 5.10 shows the cross-section of a slice before and after registration by all the algorithms. The actual values for the dataset as presented previously in the box plots are presented in Tables 5.3, 5.4, 5.5. For the 3D datasets, we use only the best performing algorithm from our family of algorithms as the benchmark, i.e. ODECME with RK4 and CME.

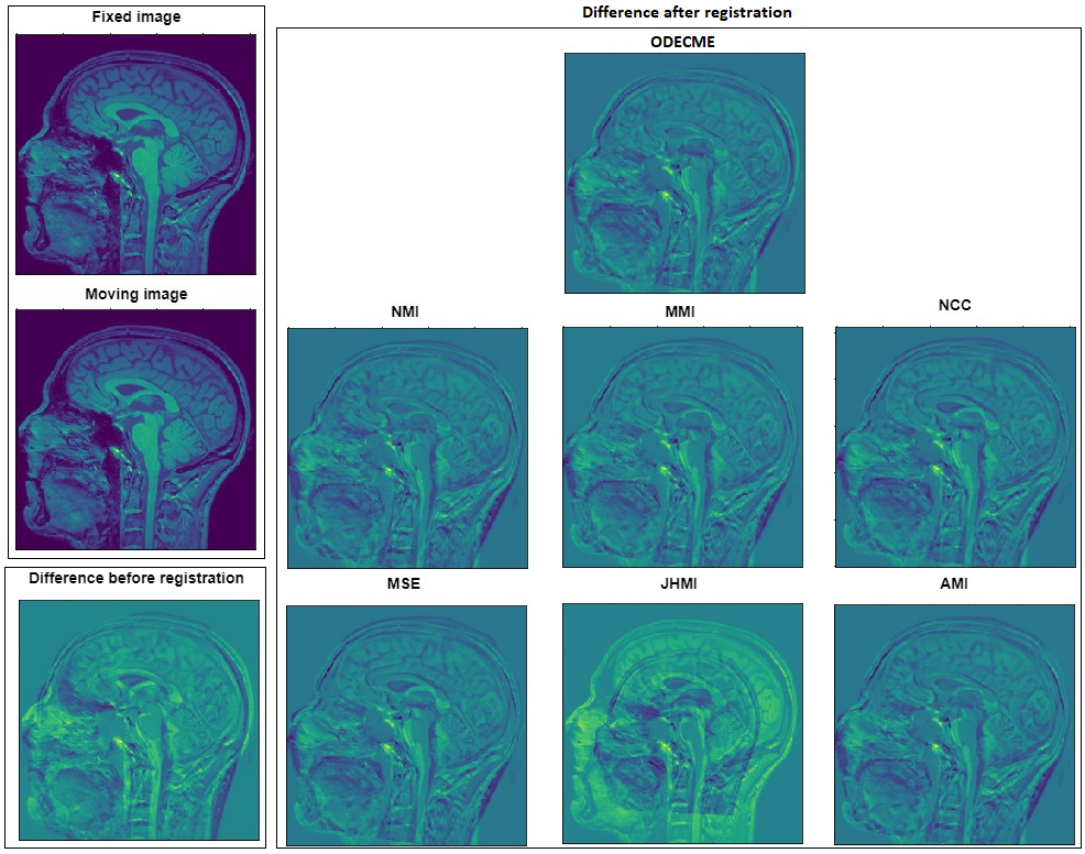

Figure 5.10: The images on the left show the middle slice of a pair of volumes to be registered from the IXI dataset. The images on the right represent the difference between the middle slices of the transformed moving volume and the fixed volume after registration by different algorithms.

Table 5.3: SSIM for IXI dataset along with paired t-test significance values

Algorithm	SSIM (Mean ± STD)	p-value
ODE (RK4-Complex)	**0.698897** ± 0.043251	-
NMI	0.676213 ± 0.039430	7.22e-08
AMI	0.673859 ± 0.041827	1.03e-20
NCC	0.665657 ± 0.043032	6.95e-21
MSE	0.652308 ± 0.040589	9.04e-19
JHMI	0.644142 ± 0.036340	6.20e-22
MMI	0.580596 ± 0.048000	6.04e-26

Table 5.4: PSNR for IXI dataset along with paired t-test significance values

Algorithm	PSNR (Mean ± STD)	p-value
ODE (RK4-Complex)	**20.652895** ± 2.700216	-
NMI	19.451672 ± 2.534976	1.85e-05
MMI	19.266031 ± 1.623640	6.97e-28
NCC	19.183119 ± 2.655105	6.78e-26
AMI	18.999632 ± 1.437429	1.49e-20
MSE	18.938889 ± 2.410362	7.93e-24
JHMI	18.417178 ± 2.100850	7.56e-08

Table 5.5: MSE for IXI dataset along with paired t-test significance values

Algorithm	MSE (Mean ± STD)	-
ODE (RK4-Complex)	**0.010224** ± 0.005447	-
JHMI	0.012630 ± 0.004336	8.22e-08
NCC	0.013196 ± 0.006556	3.41e-18
MMI	0.014214 ± 0.007280	2.34e-17
MSE	0.014594 ± 0.006722	3.86e-22
AMI	0.015413 ± 0.005074	3.71e-05
NMI	0.015845 ± 0.004178	7.91e-07

For the ADNI dataset, we look at the SSIM and PSNR values post-registration in Figures 5.11,5.12 and Tables 5.7, 5.6.

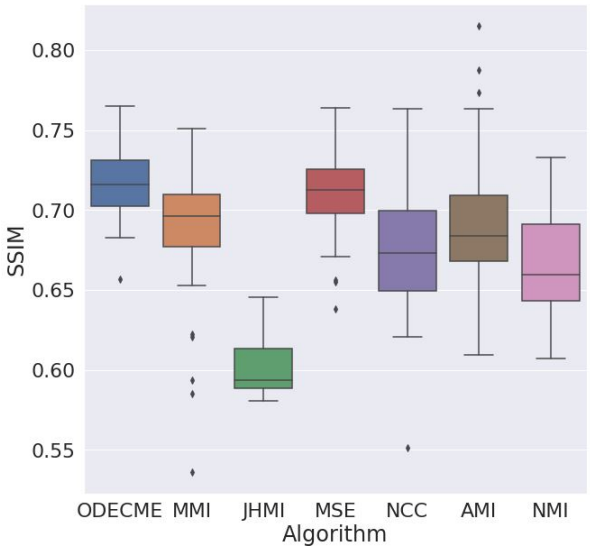

Figure 5.11: Box plot for SSIM values (higher is better) for each algorithm on the ADNI dataset after registration. ODECME refers to ODE (RK4-Complex).

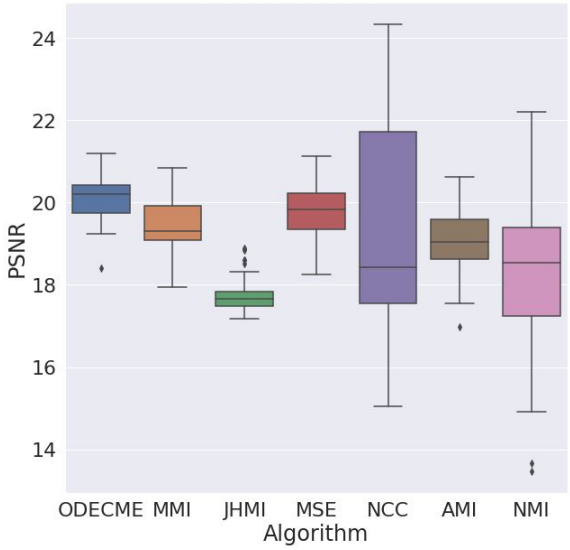

Figure 5.12: Box plot for PSNR values (higher is better) for each algorithm on the ADNI dataset after registration. ODECME refers to ODE (RK4-Complex).

Table 5.6: SSIM for ADNI dataset along with paired t-test significance values

Algorithm	SSIM (Mean ± STD)	p-value
ODE (RK4-Complex)	**0.716824** ± 0.020805	-
MSE	0.708778 ± 0.024048	0.000267
AMI	0.691885 ± 0.040358	0.0006864
MMI	0.687028 ± 0.038504	4.33e-09
NCC	0.676213 ± 0.039430	3.82e-09
NMI	0.665249 ± 0.031078	3.54e-14
JHMI	0.600950 ± 0.019171	6.20e-22

Table 5.7: PSNR for ADNI dataset along with paired t-test significance values

Algorithm	PSNR (Mean ± STD)	p-value
ODE (RK4-Complex)	**20.133869** ± 0.550024	-
MSE	19.801862 ± 0.533838	5.22e-10
NCC	19.451672 ± 2.534976	0.00657
MMI	19.409420 ± 0.612595	3.73e-17
AMI	19.092219 ± 0.790758	2.79e-10
NMI	18.228307 ± 1.795898	3.36e-09
JHMI	17.762530 ± 0.433996	9.46e-28

5.4 Ablation study

In this section we perform several ablation studies to have an understanding of the roles of all the components used in DRMIME and ODECME, such as multi-resolution pyramids, matrix exponential, complex matrix exponential, ODE and smart feature selection via Canny edge detection. We compare the performance of DRMIME/ODECME to versions of it without using the aforementioned components. For all experiments, we again perform a paired t-test between the with and without versions and report the p-value to check for statistical significance.

5.4.1 Effect of multi-resolution

All hyperparameters are kept the same in the with and without experiments, the only difference being in the with multi-resolution experiment we use 6 levels of the Gaussian pyramids in the DRMIME algorithm, whereas in the without experiment we have a single level which is the native resolution of the image. Table 5.8 lists the results for these experiments.

Table 5.8: NAED for DRMIME with and without using multi-resolution pyramids. P-value is from paired t-test between both cases.

Dataset	**DRMIME**	**Without MultiRes**	**p-value**
FIRE	0.0048 ± 0.014	**0.0043** ± 0.014	0.365
ANHIR	**0.0384** ± 0.087	0.1089 ± 0.150	1.78e-15

While the idea of multi-resolution was introduced in image registration to facilitate optimization, we note that many of the off-the-shelf algorithms have the same learning rate for all levels. As we are working with only an approximation of the distribution of the original data at different levels of the pyramid, there is a small chance that optimization at a particular sublevel could diverge. This leads to poor registration results occasionally. In our implementation of DRMIME, we produce batches which include data from all levels of the pyramid, making the optimization process much more robust,

faster and less prone to divergence. Fig. 5.4 provides evidence to this since very few results fall outside the interquartile range (as comapared to other algorithms).

5.4.2 Effect of matrix exponentiation

All hyperparameters are again kept the same in the with and without experiments; the only difference being, that rather than using a matrix exponential based parametrization, we now have 6 parameters indicating the degrees of freedom of an affine transform in a transformation matrix, i.e.

$$\begin{bmatrix} \theta_1 & \theta_2 & \theta_3 \\ \theta_4 & \theta_5 & \theta_6 \\ 0 & 0 & 1 \end{bmatrix}.$$

Table 5.9: NAED for MINE with and without using manifolds. P-value is from paired t-test between both cases.

Dataset	**DRMIME**	**Without Manifolds**	**p-value**
FIRE	0.0048 ± 0.014	**0.0045** ± 0.015	0.4933
ANHIR	**0.0384** ± 0.087	0.0580 ± 0.134	0.0012

Table 5.9 presents the results for these experiments. While the ablation study on the FIRE dataset results in similar results, the p-values from the paired t-test tells us that the results are not very significant to be able to conclude anything. The ANHIR datset on the other hand sees a statistically significant improvement with use of matrix exponentiation.

5.4.3 Effect of Sampling strategy

It could be argued that our smart feature extraction via Canny edge detection helps DRMIME perform better than other algorithms, since other algorithms do not have such custom feature detectors embedded in their pipeline. In order to reduce this potential confounding variable, we also assessed the performance of DRMIME with random sampling as well to make a fair comparison.

Table 5.10: NAED for DRMIME with Canny edge detection and Random Sampling (10%). P-value is from paired t-test between both cases.

Dataset	**With Canny**	**Random Sampling(10%)**	**p-value**
FIRE	**0.0048** $\pm$ 0.014	0.0097 $\pm$ 0.026	0.0296
ANHIR	**0.0384** $\pm$ 0.087	0.0588 $\pm$ 0.167	0.0333

Table 5.10 presents these results. As can be seen, there is a small drop in performance, but DRMIME still performs better than all the algorithms from other registration toolboxes with FIRE (Table 5.1) and better than most other algorithms with ANHIR (Table 5.2). It is important to note, that DRMIME results are using only 10% sampling, whereas the other algorithms use 50% sampling (see Appendix) due to limited memory available on the GPU.

5.4.4 Effect of CME

In order to understand how using complex matrix exponentials affect our algorithm empirically, we performed an ablation study. While the NAED performance results between DRMIME(Real) and DRMIME(Complex) in Tables 5.2 and 5.4 were not statistically significant to be able to conclusively conclude better accuracy, it does indeed speed up convergence. For instance, with real matrix exponential, for the FIRE dataset, it takes about 500 epochs to converge, while with ANHIR it takes about 1500 epochs. In case of complex matrix exponential, it only takes about 300 epochs in case of FIRE, and about 1300 epochs for ANHIR. Figure 5.16 shows the NAED convergence graphs for 10 randomly selected pairs from FIRE.

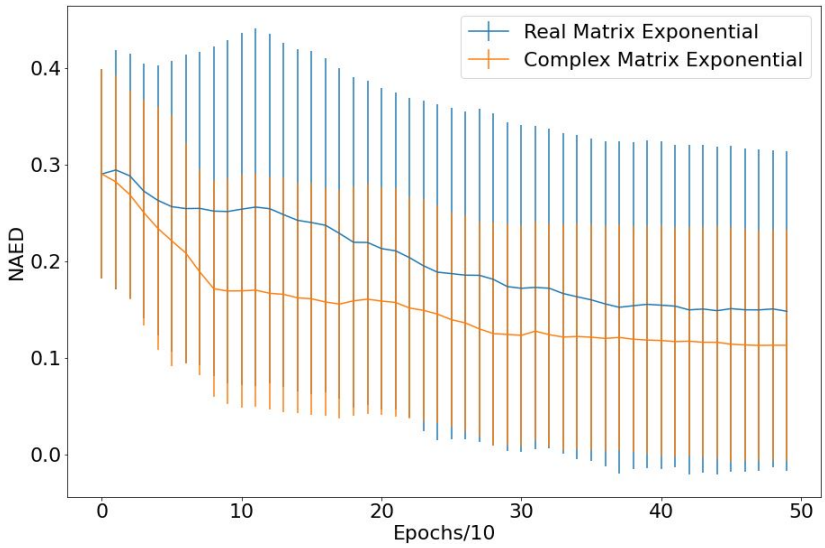

Figure 5.16: NAED averaged for 10 randomly selected pairs from FIRE, plotted over 500 epochs. The error bars represent the standard deviation.

5.4.5 Effect of ODE

To demonstrate that the ODECME Algorithm (Algorithm 3) can indeed fine-tune transformation matrices over the resolution levels, Fig. 5.17 shows variations of 6 coefficients generated by the ODE over different resolution levels. These coefficients were obtained by registering a pair of images from the FIRE dataset. It shows that the proposed ODE can adapt to the needs of the edges and structures as they are shifted in the Gaussian pyramids.

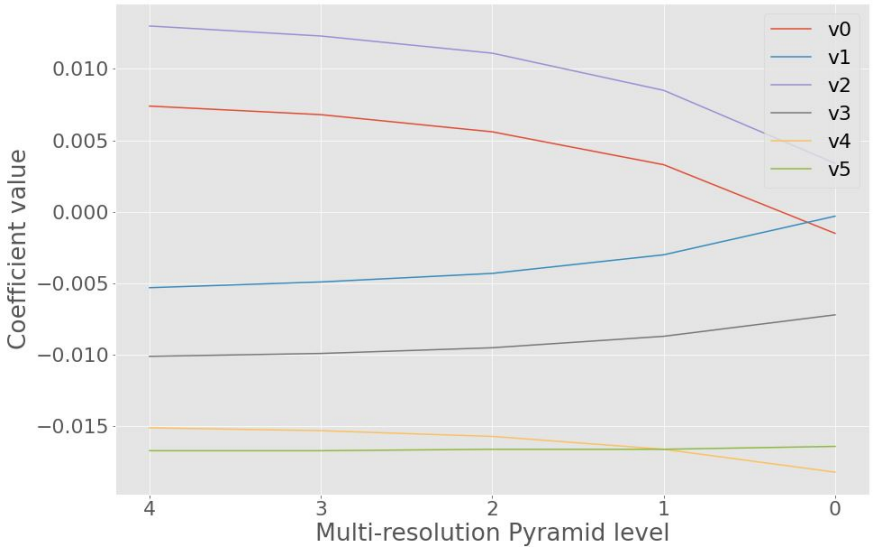

Figure 5.17: Plot showing how individual coefficients generated by ODEnet vary with successive resolution levels. Level 0 is the original image and 4 denotes the coarsest resolution.

Table 5.11 shows that for every matrix exponential coefficient (real and imaginary) varies over a range. The average was computed over the range of a coefficient across all image pairs after registration.

Table 5.11: The average range and standard deviation of real and imaginary coefficients after registering the FIRE dataset

Coefficient	(Real) Mean Range ± SD	(Imag.) Mean Range ± SD
v_0	5.772e-03 ± 5.516e-03	5.771e-03 ± 5.515e-03
v_1	9.540e-03 ± 8.420e-03	9.537e-03 ± 8.414e-03
v_2	5.745e-03 ± 5.479e-03	5.745e-03 ± 5.476e-03
v_3	8.796e-03 ± 9.861e-03	8.796e-03 ± 9.854e-03
v_4	5.657e-03 ± 5.090e-03	5.664e-03 ± 5.088e-03
v_5	6.951e-03 ± 4.716e-03	7.068e-03 ± 4.796e-03

5.5 Efficiency

For efficiency we look at two perspectives: time efficiency and accuracy. On a set of 10 randomly selected images (the set remains the same across all algorithms) from the FIRE dataset, we run a set of experiments for all the

algorithms. We report the registration accuracy in terms of the ground truth (NAED) of these 10 images. The hardware for these experiments was NVIDIA GeForce GTX 1080 Ti, Intel(R) Xeon(R) CPU E5-2620 v4 @ 2.10GHz, 32GB RAM.

For time efficiency, we run each algorithm for 1000 epochs, report the time taken and the accuracy achieved. The number of epochs was chosen as an upper limit number by when every algorithm had converged. The time taken tells us the fastest algorithm among those being considered, and also at the same time, its accuracy should at least be on par with other slower algorithms.

Table 5.12: Time taken for 1000 epochs and resultant NAED (lower is better)

Algorithm	Time (seconds)	NAED
ODECME (RK4) (50 epochs)	108	0.01921
NMI	60	0.02503
AMI	620	0.02942
ODECME (RK4)	1601	0**0.00360**
MMI	2904	0.00598
JHMI	1859	0.00605
NCC	3804	0.00697
MSE	2847	0.02918

From Table 5.12, we can infer that while our algorithm attains the best NAED, it ranks third in terms of time taken to execute 1000 epochs. While AMI and NMI are faster, they are almost an order of magnitude worse in terms of the NAED performance.

Since this a tradeoff between time and efficiency, ODECME can perform extremely well at both ends of the spectrum. For instance, while individual epochs on AMI and NMI might be faster, we can achieve comparable accuracy by running ODECME for much less epochs; within 50 epochs of optimization ODECME achieves an NAED of 0.01921 taking only 108 seconds, which is better than AMI and NMI over a 1000 epochs. The reason for a single epoch taking longer for ODECME can be attributed to the fact that it works with batched data from multiple-resolutions.

Also as a note, only ODECME/DRMIME and AMI are GPU compatible, while the remaining were run on CPU.

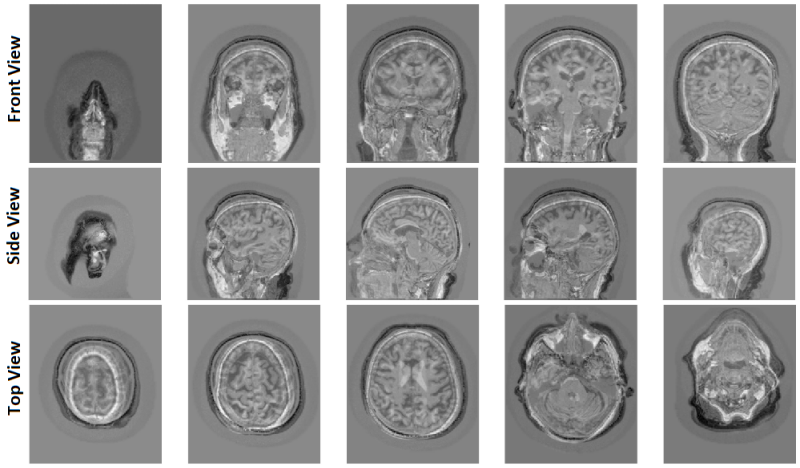

Figure 5.13: Randomly selected slices from the difference volume before registration between the reference and a randomly moving volume from the ADNI dataset. Each row represents slices from a different axis.

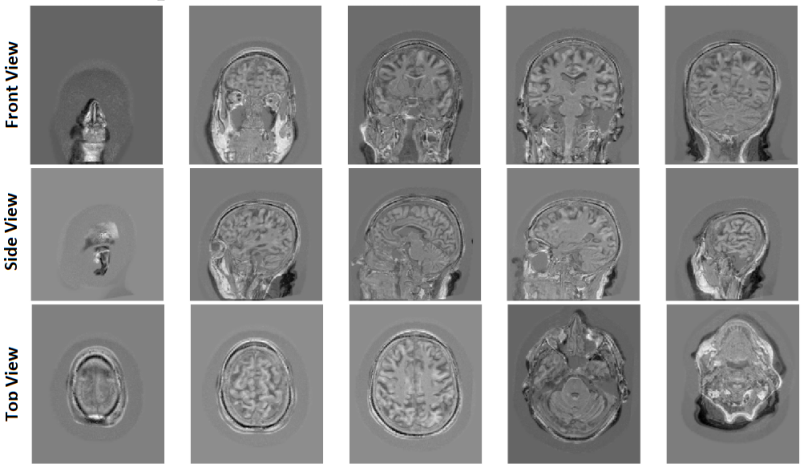

Figure 5.14: Same slices from the difference volume after registration using ODECME.

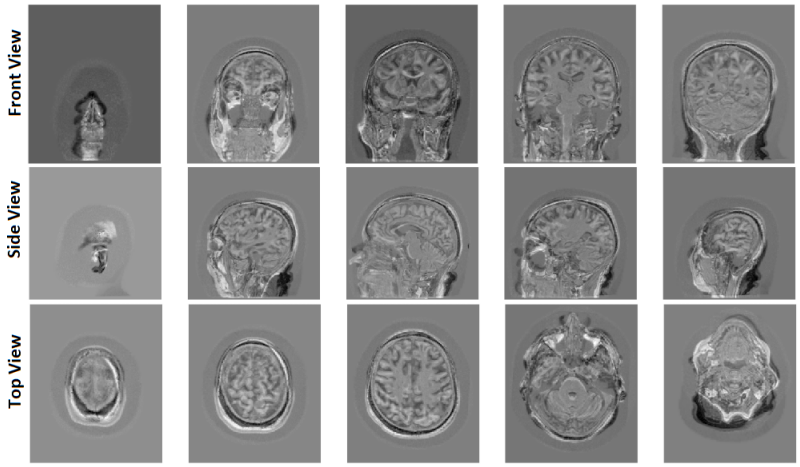

Figure 5.15: Same slices from the difference volume after registration using MSE.

Chapter 6

Conclusion

Optimization-based image registration using homography as a transformation is classical. However, recent toolboxes with autograd capability and strong GPU acceleration has created opportunity to improve this classical registration algorithms. In this work, we show that using complex matrix exponential convergence can be accelerated for such algorithms. Also using ordinary differential equation, we can further refine the accuracy of such algorithms for multi-resolution image registration problems that is able to employ any differentiable objective function. Our algorithm yields state-of-the-art accuracy for benchmark 2D and 3D datasets.

References

[1] airlab. *airlab*. URL: `https://github.com/airlab-unibas/airlab` (visited on 07/31/2020).

[2] Haikel Salem Alhichri and Mohamed Kamel. "Multi-resolution image registration using multi-class Hausdorff fraction."
In: *Pattern recognition letters* 23.1-3 (2002), pp. 279–286.

[3] Yali Amit. "Graphical shape templates for automatic anatomy detection with applications to MRI brain scans."
In: *IEEE Transactions on Medical Imaging* 16.1 (1997), pp. 28–40.

[4] Simon Baker and Iain Matthews.
"Lucas-kanade 20 years on: A unifying framework."
In: *International journal of computer vision* 56.3 (2004), pp. 221–255.

[5] Arindam Banerjee. "On bayesian bounds." In: *Proceedings of the 23rd international conference on Machine learning*. 2006, pp. 81–88.

[6] Herbert Bay, Tinne Tuytelaars, and Luc Van Gool.
"Surf: Speeded up robust features."
In: *European conference on computer vision*. Springer. 2006, pp. 404–417.

[7] Erik Johannes Bekkers et al.
"Template matching via densities on the roto-translation group."
In: *IEEE transactions on pattern analysis and machine intelligence* 40.2 (2017), pp. 452–466.

[8] Mohamed Ishmael Belghazi et al.
"Mine: mutual information neural estimation."
In: *arXiv preprint arXiv:1801.04062* (2018).

[9] FL Bookstein and WDK Green.
"A thin-plate spline and the decomposition of deformations."
In: *Mathematical Methods in Medical Imaging* 2 (1993), pp. 14–28.

[10] Jiři Borovec et al. "ANHIR: automatic non-rigid histological image registration challenge."
In: *IEEE Transactions on Medical Imaging* (2020).

[11] J.C Butcher. *Numerical Methods for Ordinary Differential Equations*. Willy Online Library, 2016. URL: https://onlinelibrary.wiley.com/doi/book/10.1002/9781119121534.

[12] Ali Can et al. "A feature-based, robust, hierarchical algorithm for registering pairs of images of the curved human retina." In: *IEEE transactions on pattern analysis and machine intelligence* 24.3 (2002), pp. 347–364.

[13] John Canny. "A computational approach to edge detection." In: *IEEE Transactions on pattern analysis and machine intelligence* 6 (1986), pp. 679–698.

[14] Wisarut Chantara et al. "Object tracking using adaptive template matching." In: *IEIE Transactions on Smart Processing and Computing* 4.1 (2015), pp. 1–9.

[15] Xi Cheng, Li Zhang, and Yefeng Zheng. "Deep similarity learning for multimodal medical images." In: *Computer Methods in Biomechanics and Biomedical Engineering: Imaging & Visualization* 6.3 (2018), pp. 248–252.

[16] André Collignon et al. "3D multi-modality medical image registration using feature space clustering." In: *International Conference on Computer Vision, Virtual Reality, and Robotics in Medicine*. Springer. 1995, pp. 195–204.

[17] Malcolm H Davis et al. "A physics-based coordinate transformation for 3-D image matching." In: *IEEE transactions on medical imaging* 16.3 (1997), pp. 317–328.

[18] Daniel DeTone, Tomasz Malisiewicz, and Andrew Rabinovich. "Deep image homography estimation." In: *arXiv preprint arXiv:1606.03798* (2016).

[19] Monroe D Donsker and SR Srinivasa Varadhan. "Asymptotic evaluation of certain Markov process expectations for large time, I." In: *Communications on Pure and Applied Mathematics* 28.1 (1975), pp. 1–47.

[20] Ethan Eade. "Lie groups for 2d and 3d transformations." In: *URL http://ethaneade. com/lie. pdf, revised Dec* 117 (2013), p. 118.

[21] Marwa Elbouz et al. "Correlation based efficient face recognition and color change detection." In: *Optics Communications* 311 (2013), pp. 186–200.

[22] Georgios D Evangelidis and Emmanouil Z Psarakis. "Parametric image alignment using enhanced correlation coefficient maximization." In: *IEEE Transactions on Pattern Analysis and Machine Intelligence* 30.10 (2008), pp. 1858–1865.

[23] Martin A Fischler and Robert C Bolles.
"Random sample consensus: a paradigm for model fitting with applications to image analysis and automated cartography."
In: *Communications of the ACM* 24.6 (1981), pp. 381–395.

[24] Jean Gallier and Jocelyn Quaintance.
Differential Geometry and Lie Groups A Computational Perspective.
Springer International Publishing, 2020.
DOI: 10.1007/978-3-030-46040-2.
URL: https://www.seas.upenn.edu/~jean/diffgeom-spr-I.pdf.

[25] Leopoldo N Gaxiola et al.
"Target tracking with dynamically adaptive correlation."
In: *Optics Communications* 365 (2016), pp. 140–149.

[26] Yaorong Ge et al. "Intersubject brain image registration using both cortical and subcortical landmarks."
In: *Medical Imaging 1995: Image Processing*. Vol. 2434.
International Society for Optics and Photonics. 1995, pp. 81–95.

[27] Izrail Moiseevitch Gelfand, Richard A Silverman, et al.
Calculus of variations. Courier Corporation, 2000.

[28] Sayan Ghosal and Nilanjan Ray. "Deep deformable registration: Enhancing accuracy by fully convolutional neural net."
In: *Pattern Recognition Letters* 94 (2017), pp. 81–86.

[29] Andrea Grosso et al.
"Hypertensive retinopathy revisited: some answers, more questions."
In: *British Journal of Ophthalmology* 89.12 (2005), pp. 1646–1654.

[30] Shao-Ya Guan et al.
"A review of point feature based medical image registration."
In: *Chinese Journal of Mechanical Engineering* 31.1 (2018), p. 76.

[31] Carlos Hernandez-Matas et al.
"FIRE: fundus image registration dataset."
In: *Journal for Modeling in Ophthalmology* 1.4 (2017), pp. 16–28.

[32] Derek LG Hill et al.
"A strategy for automated multimodality image registration incorporating anatomical knowledge and imager characteristics."
In: *Biennial International Conference on Information Processing in Medical Imaging*. Springer. 1993, pp. 182–196.

[33] Derek LG Hill et al. "Medical image registration."
In: *Physics in medicine & biology* 46.3 (2001), R1.

[34] Michal Irani and P Anandan. "Robust multi-sensor image alignment."
In: *Sixth International Conference on Computer Vision (IEEE Cat. No. 98CH36271)*. IEEE. 1998, pp. 959–966.

[35] ITK. *itk::JointHistogramMutualInformationImageToImageMetricv4*. URL: https://itk.org/Doxygen/html/classitk_1_1JointHistogramMutualInformationImageToImageMetricv4.html (visited on 09/12/2010).

[36] ITK. *itk::MattesMutualInformationImageToImageMetricv4*. URL: https://itk.org/Doxygen/html/classitk_1_1MattesMutualInformationImageToImageMetricv4.html (visited on 09/12/2010).

[37] ITK. *itk::MeanSquaresImageToImageMetricv4*. URL: https://itk.org/Doxygen/html/classitk_1_1MeanSquaresImageToImageMetricv4.html (visited on 09/12/2010).

[38] ITK. *itk::NormalizedCorrelationImageToImageMetric*. URL: https://itk.org/Doxygen/html/classitk_1_1NormalizedCorrelationImageToImageMetric.html (visited on 09/12/2010).

[39] Yan Ke and Rahul Sukthankar. "PCA-SIFT: A more distinctive representation for local image descriptors." In: *Proceedings of the 2004 IEEE Computer Society Conference on Computer Vision and Pattern Recognition, 2004. CVPR 2004.* Vol. 2. IEEE. 2004, pp. II–II.

[40] Vladimir V Kisil. *Geometry of Möbius Transformations*. World Scientific, 2012.

[41] Stefan Klein and Marius Staring. *itk::AdvancedImageToImageMetric*. URL: http://elastix.isi.uu.nl/doxygen/classitk_1_1AdvancedImageToImageMetric.html (visited on 09/12/2010).

[42] Stefan Klein et al. "Adaptive stochastic gradient descent optimisation for image registration." In: *International journal of computer vision* 81.3 (2009), p. 227.

[43] Stefan Krüger and Andrew Calway. "Image Registration using Multiresolution Frequency Domain Correlation." In: *BMVC*. 1998, pp. 1–10.

[44] Kenneth Levenberg. "A method for the solution of certain non-linear problems in least squares." In: *Quarterly of applied mathematics* 2.2 (1944), pp. 164–168.

[45] Tsung-Yi Lin et al. "Microsoft coco: Common objects in context." In: *European conference on computer vision*. Springer. 2014, pp. 740–755.

[46] David G Lowe. "Object recognition from local scale-invariant features." In: *Proceedings of the seventh IEEE international conference on computer vision*. Vol. 2. Ieee. 1999, pp. 1150–1157.

[47] Bruce D Lucas, Takeo Kanade, et al. "An iterative image registration technique with an application to stereo vision." In: (1981).

[48] Simon Lucey et al. "Fourier lucas-kanade algorithm." In: *IEEE transactions on pattern analysis and machine intelligence* 35.6 (2012), pp. 1383–1396.

[49] Frederik Maes et al. "Multimodality image registration by maximization of mutual information." In: *IEEE transactions on Medical Imaging* 16.2 (1997), pp. 187–198.

[50] David Mattes et al. "Nonrigid multimodality image registration." In: *Medical Imaging 2001: Image Processing*. Vol. 4322. International Society for Optics and Photonics. 2001, pp. 1609–1620.

[51] David Mattes et al. "PET-CT image registration in the chest using free-form deformations." In: *IEEE transactions on medical imaging* 22.1 (2003), pp. 120–128.

[52] Cleve Moler and Charles Van Loan. "Nineteen dubious ways to compute the exponential of a matrix, twenty-five years later." In: *SIAM review* 45.1 (2003), pp. 3–49.

[53] Enrique Muñoz, Pablo Márquez-Neila, and Luis Baumela. "Rationalizing efficient compositional image alignment." In: *International Journal of Computer Vision* 112.3 (2015), pp. 354–372.

[54] Abhishek Nan et al. "DRMIME: Differentiable Mutual Information and Matrix Exponential for Multi-Resolution Image Registration." In: *MIDL 2020 Conference*. 2020. URL: https://openreview.net/forum?id=Q0Bm5e6dkW (visited on 06/25/2020).

[55] Ty Nguyen et al. "Unsupervised deep homography: A fast and robust homography estimation model." In: *IEEE Robotics and Automation Letters* 3.3 (2018), pp. 2346–2353.

[56] Adam Paszke et al. "PyTorch: An Imperative Style, High-Performance Deep Learning Library." In: *Advances in Neural Information Processing Systems 32*. Ed. by H. Wallach et al. Curran Associates, Inc., 2019, pp. 8024–8035. URL: http://papers.neurips.cc/paper/9015-pytorch-an-imperative-style-high-performance-deep-learning-library.pdf.

[57] J. P. W. Pluim, J. B. A. Maintz, and M. A. Viergever. "Mutual-information-based registration of medical images: a survey." In: *IEEE Transactions on Medical Imaging* 22.8 (Aug. 2003), pp. 986–1004. ISSN: 1558-254X. DOI: 10.1109/TMI.2003.815867.

[58] Josien PW Pluim, JB Antoine Maintz, and Max A Viergever. "Mutual information matching in multiresolution contexts." In: *Image and Vision Computing* 19.1-2 (2001), pp. 45–52.

[59] Josien PW Pluim, JB Antoine Maintz, and Max A Viergever. "Mutual-information-based registration of medical images: a survey." In: *IEEE transactions on medical imaging* 22.8 (2003), pp. 986–1004.

[60] Ethan Rublee et al. "ORB: An efficient alternative to SIFT or SURF." In: *2011 International conference on computer vision*. Ieee. 2011, pp. 2564–2571.

[61] Robin Sandkühler et al. "AirLab: Autograd Image Registration Laboratory." In: *CoRR* abs/1806.09907 (2018). arXiv: 1806.09907. URL: http://arxiv.org/abs/1806.09907.

[62] Martin Schröter, Uwe Helmke, and Otto Sauer. "A Lie-Group Approach to Rigid Image Registration." In: *arXiv preprint arXiv:1007.5160* (2010).

[63] scikit-image. *skimage.metrics.peak$_s$ignal$_n$oise$_r$atio*. URL: https://scikit-image.org/docs/stable/api/skimage.metrics.html#skimage.metrics.peak_signal_noise_ratio (visited on 07/31/2020).

[64] scikit-image. *skimage.metrics.structural$_s$imilarity*. URL: https://scikit-image.org/docs/stable/api/skimage.metrics.html#skimage.metrics.structural_similarity (visited on 07/31/2020).

[65] Mayur Sevak and Amit Choksi. *A Survey of Feature Based Image Registration Algorithms: Performance Evaluation of SIFT Algorithm*. Mar. 2016. DOI: 10.13140/RG.2.1.3724.4566.

[66] simpleelastix. *simpleelastix*. URL: https://simpleelastix.github.io/ (visited on 07/31/2020).

[67] SimpleITK. *SimpleITK*. URL: https://simpleitk.org/ (visited on 07/31/2020).

[68] Colin Studholme, Derek LG Hill, and David J Hawkes. "An overlap invariant entropy measure of 3D medical image alignment." In: *Pattern recognition* 32.1 (1999), pp. 71–86.

[69] Colin Studholme, Derek LG Hill, and David J Hawkes. "Multiresolution voxel similarity measures for MR-PET registration." In: *Information processing in medical imaging*. Vol. 3. Dordrecht, The Netherlands: Kluwer. 1995, pp. 287–298.

[70] Gérard Subsol, Jean-Philippe Thirion, and Nicholas Ayache. "A scheme for automatically building 3D morphometric anatomical atlases: application to a skull atlas." In: (1998).

[71] Wei Sun et al. “Simultaneous multiresolution strategies for nonrigid image registration.” In: *IEEE Transactions on Image Processing* 22.12 (2013), pp. 4905–4917.

[72] Richard Szeliski. “Image alignment and stitching: A tutorial.” In: *Foundations and Trends® in Computer Graphics and Vision* 2.1 (2006), pp. 1–104.

[73] Richard Szeliski and Stéphane Lavallée. “Matching 3-D anatomical surfaces with non-rigid deformations using octree-splines.” In: *International journal of computer vision* 18.2 (1996), pp. 171–186.

[74] Camillo J Taylor and David J Kriegman. “Minimization on the Lie group SO (3) and related manifolds.” In: *Yale University* 16.155 (1994), p. 6.

[75] Philippe Thevenaz, Urs E Ruttimann, and Michael Unser. “A pyramid approach to subpixel registration based on intensity.” In: *IEEE transactions on image processing* 7.1 (1998), pp. 27–41.

[76] Philippe Thévenaz and Michael Unser. “Optimization of mutual information for multiresolution image registration.” In: *IEEE transactions on image processing* 9.ARTICLE (2000), pp. 2083–2099.

[77] Alain Trouvé. “Diffeomorphisms groups and pattern matching in image analysis.” In: *International journal of computer vision* 28.3 (1998), pp. 213–221.

[78] Andrea Valsecchi et al. “Intensity-based image registration using scatter search.” In: *Artificial intelligence in medicine* 60.3 (2014), pp. 151–163.

[79] Paul Viola and William M Wells III. “Alignment by maximization of mutual information.” In: *International journal of computer vision* 24.2 (1997), pp. 137–154.

[80] Christian Wachinger and Nassir Navab. “Simultaneous registration of multiple images: Similarity metrics and efficient optimization.” In: *IEEE transactions on pattern analysis and machine intelligence* 35.5 (2012), pp. 1221–1233.

[81] William M Wells III et al. “Multi-modal volume registration by maximization of mutual information.” In: *Medical image analysis* 1.1 (1996), pp. 35–51.

[82] A. Witkin. “Scale-space filtering: A new approach to multi-scale description.” In: *ICASSP ’84. IEEE International Conference on Acoustics, Speech, and Signal Processing*. Vol. 9. 1984, pp. 150–153.

[83] Roger P Woods, Simon R Cherry, and John C Mazziotta. “Rapid automated algorithm for aligning and reslicing PET images.” In: *Journal of computer assisted tomography* 16.4 (1992), pp. 620–633.

[84] Jue Wu and Albert CS Chung. "Multimodal brain image registration based on wavelet transform using SAD and MI."
In: *International Workshop on Medical Imaging and Virtual Reality*. Springer. 2004, pp. 270–277.

[85] Bradley T Wyman et al. "Standardization of analysis sets for reporting results from ADNI MRI data."
In: *Alzheimer's & Dementia* 9.3 (2013), pp. 332–337.

[86] Qing Yan et al. "HEASK: Robust homography estimation based on appearance similarity and keypoint correspondences."
In: *Pattern Recognition* 47.1 (2014), pp. 368–387.

Appendix A

A.1 DV Lower Bound Reaches Mutual Information

MINE maximizes the DV lower bound (2.11) with respect to a function $f(x, z)$. Let us consider a perturbation function $g(x, z)$ and the perturbed objective function $J(f + \epsilon g)$ for a small number ϵ. Taking the following limit (using LHospitals rule), we obtain:

$$\lim_{\epsilon \to 0} \frac{J(f + \epsilon g) - J(f)}{\epsilon} = \int g(x, z) P_{XZ}(x, z) dxdz - \int g(x, z) \frac{exp(f(x, z)) P_X(x) P_Z(z)}{\int exp(f(x, z)) P_X(x) P_Z(z) dxdz}] dxdz. \tag{A.1}$$

Using principles of calculus of variations[27], this limit should be 0 for J to achieve an extremum. Since perturbation function $g(x, z)$ is arbitrary, this condition is possible only when

$$P_{XZ}(x, z) = \frac{exp(f(x, z)) P_X(x) P_Z(z)}{\int exp(f(x, z)) P_X(x) P_Z(z) dxdz}, \tag{A.2}$$

i.e., the Gibbs density [8] is achieved. From (A.2), we obtain:

$$f(x, z) = log(\frac{P_{XZ}(x, z)}{P_X(x) P_Z(z)} \int exp(f(x, z)) P_X(x) P_Z(z) dxdz). \tag{A.3}$$

Using this expression in equation (2.11), we obtain:

$$J(f) = \int P_{XZ}(x, z) log \frac{P_{XZ}(x, z)}{P_X(x) P_Z(z)} dxdz = MI. \tag{A.4}$$

Thus, maximization of $J(f)$ leads to mutual information.

A.2 Algorithm Hyperparameters

All architectures and hyper-parameters for our experiments are listed here (In case a hyperparameter isn't mentioned, its default value provided by the framework was used):

A.2.1 DRMIME

: Our implementation of the network f_θ for MINE uses a fully connected network with twice the number of input channels as the input layer, e.g., for a color image it is $3 \times 2 = 6$. There are two hidden layers with 100 neurons in each and the output layer has a scalar output. Apart from the output layer which has no activation, ReLU activation is used.

1. learningRate:
    - FIRE/ANHIR: $\alpha = 1e-2$, $\beta = 1e-3$, $\gamma = 1e-4$
2. numberOfIterations: 500 (FIRE)/1500 (ANHIR)
3. Optimizer : ADAM with AMSGRAD

A.2.2 ODECME

: MINE implementation is identical to DRMIME.

For ODE, the input layer for g_ϕ consists of 7 and 8 neurons in case of FIRE/ANHIR and IXI/ADNI, respectively. The reasoning being, that one neuron accounts for the scale of the level in the Gaussian pyramid and remaining neurons are for the number of matrix exponential coefficients (6 for 2D and 7 for 3D datasets in our experiments). We use the same network separately for the real and the imaginary coefficients. It has a single hidden layer comprising of 100 neurons and the final output layer consists of neurons equal to the number of matrix exponential coefficients. All layers have ReLU activation, except for the final layer.

1. learningRate:

- FIRE/ANHIR: $\alpha = 1e-2$, $\beta = 1e-3$, $\gamma = 1e-4$
- ADNI/IXI: $\alpha = 1e-1$, $\beta = 1e-2$, $\gamma = 1e-2$

2. numberOfIterations: 300 (FIRE)/1300 (ANHIR)/500 (ADNI)/ 500 (IXI)
3. Optimizer : ADAM with AMSGRAD
4. SamplingPercentage: 0.1

A.2.3 MMI

:

1. learningRate: 1e-5 (FIRE/ANHIR), 1e-1 (ADNI/IXI)
2. numberOfIterations: 5000 (FIRE/ANHIR), 1500 (ADNI/IXI)
3. numberOfHistogramBins: 100
4. convergenceMinimumValue: 1e-9
5. convergenceWindowSize: 200
6. SamplingStrategy: Random
7. SamplingPercentage: 0.5

A.2.4 JHMI

:

1. learningRate: 1e-1 (FIRE/ANHIR), 1e-1 (ADNI/IXI)
2. numberOfIterations: 5000 (FIRE/ANHIR), 1500 (ADNI/IXI)
3. numberOfHistogramBins: 100
4. convergenceMinimumValue: 1e-9
5. convergenceWindowSize: 200
6. SamplingStrategy: Random
7. SamplingPercentage: 0.5

A.2.5 MSE

:

1. learningRate: 1e-6 (FIRE/ANHIR), 1e-2 (ADNI/IXI)
2. numberOfIterations: 5000 (FIRE/ANHIR), 1500 (ADNI/IXI)
3. convergenceMinimumValue: 1e-9
4. convergenceWindowSize: 200

A.2.6 NCC

:

1. learningRate: 1e-1 (FIRE/ANHIR), 1e-1 (ADNI/IXI)
2. numberOfIterations: 5000 (FIRE/ANHIR), 1500 (ADNI/IXI)
3. convergenceMinimumValue: 1e-9
4. convergenceWindowSize: 200

A.2.7 NMI

:

1. numberOfIterations: 5000 (FIRE/ANHIR), 2000 (ADNI/IXI)

A.2.8 AMI

:

1. learningRate: 1e-4 (FIRE/ANHIR), 1e-1 (ADNI/IXI)
2. numberOfIterations: 5000 (FIRE/ANHIR), 1500 (ADNI/IXI)
3. Optimizer : AMSGRAD